Journal of Experimental Botany, Vol. 75, No. 13 pp. 4093–4110, 2024
https://doi.org/10.1093/jxb/erae140 Advance Access Publication 29 March 2024

RESEARCH PAPER

Modelling metabolic fluxes of tomato stems reveals that nitrogen shapes central metabolism for defence against *Botrytis cinerea*

Nathalie Lacrampe[1,2], Raphaël Lugan[1], Doriane Dumont[1], Philippe C. Nicot[4], François Lecompte[1,†,*], and Sophie Colombié[3,†]

[1] PSH unit, INRAE, F-84914 Avignon, France
[2] UMR Qualisud, Avignon Université, F-84916 Avignon, France
[3] UMR 1332 BFP, INRAE, Univ Bordeaux, F-33883 Villenave d'Ornon, France
[4] Plant Pathology Unit, INRAE, F-84140 Montfavet, France

[†] These authors contributed equally to this work.
* Correspondence: francois.lecompte.2@inrae.fr

Received 12 September 2023; Editorial decision 26 March 2024; Accepted 28 March 2024

Editor: Monica Höfte, University of Ghent, Belgium

Abstract

Among plant pathogens, the necrotrophic fungus *Botrytis cinerea* is one of the most prevalent, leading to severe crop damage. Studies related to its colonization of different plant species have reported variable host metabolic responses to infection. In tomato, high N availability leads to decreased susceptibility. Metabolic flux analysis can be used as an integrated method to better understand which metabolic adaptations lead to effective host defence and resistance. Here, we investigated the metabolic response of tomato infected by *B. cinerea* in symptomless stem tissues proximal to the lesions for 7 d post-inoculation, using a reconstructed metabolic model constrained by a large and consistent metabolic dataset acquired under four different N supplies. An overall comparison of 48 flux solution vectors of *Botrytis*- and mock-inoculated plants showed that fluxes were higher in *Botrytis*-inoculated plants, and the difference increased with a reduction in available N, accompanying an unexpected increase in radial growth. Despite higher fluxes, such as those involved in cell wall synthesis and other pathways, fluxes related to glycolysis, the tricarboxylic acid cycle, and amino acid and protein synthesis were limited under very low N, which might explain the enhanced susceptibility. Limiting starch synthesis and enhancing fluxes towards redox and specialized metabolism also contributed to defence independent of N supply.

Keywords: *Botrytis cinerea*, central metabolism, constraint-based modelling, metabolic fluxes, necrotrophic pathogens, nitrogen, tomato (*Solanum lycopersicum*).

Abbreviations: dpi, days post-inoculation; GABA, γ-aminobutyric acid; MEP/DOXP, 2-*C*-methyl-D-erythritol 4-phosphate/1-deoxy-D-xylulose 5-phosphate; PC, principal component; RGR, relative growth rate; TCA, tricarboxylic acid.

Introduction

Safe control of plant pathogens is an important issue for food security. To achieve this goal, an increased understanding of the effect of the environment on plant immunity is needed. The core of plant responses to invaders is based on several mechanisms: recognition of microbial structures, identification of host damage by pattern recognition receptors, detection of effectors, activation of signalling by various classes of kinases, ion influx and reactive oxygen species (ROS) production, and defence responses orchestrated by hormonal crosstalk (for recent reviews, see Aerts *et al*., 2021; Ngou *et al*., 2022; Wang *et al*., 2022). Successful pathogens are able to evade the first lines of plant defence, which largely depend on their available effector repertoire, as well as other toxic metabolites (Lo Presti *et al*., 2015). In the case of microbial interactions, the infected host organs produce a range of compounds to combat the spread of the disease. This metabolic activity depends on the host species and the pathogen lifestyle, and may include antimicrobial secondary metabolites, antioxidative and detoxifying compounds, polymers for strengthening the cell wall, and defence-oriented proteins.

Necrotrophic pathogens are a class of microbial agents that deploy an arsenal of toxins, cell wall-degrading enzymes, proteases, and cell death-inducing enzymes to kill cells and recover their nutrients from dead host tissues (Liao *et al*., 2022). Among necrotrophic fungi, *Botrytis cinerea* is one of the most important due to its broad host range, which includes major agronomic crops, and the severe damage it can inflict on plants, either during their cycle or after harvest (Dean *et al*., 2012). Many studies have highlighted the role of plant secondary metabolites against *B. cinerea*, which may directly inhibit fungal germination or growth or mitigate the effect of fungal virulence factors. This includes compounds of different chemical classes, whose synthesis may be specific to a botanical family or even a species. Among them are phenolic compounds (Adrian *et al*., 1997; Goetz *et al*., 1999; Iriti *et al*., 2004; Morales *et al*., 2017), terpenoids (Tsao and Zhou, 2000; Stukkens *et al*., 2005), glycoalkaloids and saponins (Quidde *et al*., 1998; You and Kan, 2021), and glucosinolates or the tryptophan-derived alkaloid camalexin (Ferrari *et al*., 2003; Kliebenstein *et al*., 2005; Buxdorf *et al*., 2013). The synthesis of these compounds requires an adaptation of the transcriptional machinery and enhanced enzymatic activity in the pathways involved.

There is ample evidence that the defence response requires an adaptation of primary metabolism, which provides basic C and N backbones as well as energy and reducing power for the synthesis of defence compounds (Bolton, 2009; Guo *et al*., 2018). Accordingly, several transcriptomic, metabolomic, and proteomic studies on various plant models and crops have shown a reprogramming of a large part of the host primary and secondary metabolism following infection by *B. cinerea*. (e.g. Rowe *et al*., 2010 and Mulema and Denby, 2012 on Arabidopsis; Hong *et al*., 2012 on vine; De Cremer *et al*., 2013 on lettuce; Camañes *et al*., 2015 and Vega *et al*., 2015 on tomato; Kumar *et al*., 2020 on chrysanthemum; and Naets *et al*., 2022 on apple). These studies confirm earlier reports (Berger *et al*., 2004) of a down-regulation, in photosynthetic organs, of the photosynthetic machinery, as well as repression of starch biosynthesis. A mobilization of the sugar pool is illustrated by the increased transcription of genes encoding invertases (Mulema and Denby, 2012; De Cremer *et al*., 2013) and, in sink tissues, sucrose synthases (Lacrampe *et al*., 2021). However, there are contradicting reports regarding the activation, following infection, of genes encoding enzymes of glycolytic or pentose-phosphate pathways or the tricarboxylic acid (TCA) cycle, along with a variable evolution, depending on the studies, of metabolite contents. Monolignols form, through oxidative coupling, lignin that accumulates in the cell wall for its reinforcement against pathogen invasion (Dixon *et al*., 2002). Flavonoids and anthocyanins are antioxidants thought to regulate the ROS burst resulting from *B. cinerea* infection that may favour fungal propagation. However, their role in controlling invasion depends on their structure, which confers specific ROS-scavenging activity (Zhang *et al*., 2015). For these secondary compounds, discrepancies in transcriptomic or metabolomic studies have also been reported. In several host species, the mevalonate pathway is up-regulated following infection (De Cremer *et al*., 2013; Smith *et al*., 2014; Naets *et al*., 2022), leading to the synthesis of some classes of terpenoids (Mulema and Denby, 2012; De Cremer *et al*., 2013; Xiong *et al*., 2018; Kumar *et al*., 2020; Badmi *et al*., 2022; Naets *et al*., 2022). Many other metabolites and metabolic routes have been shown to be affected by *B. cinerea* infection, such as fatty acids and lipids (Agudelo-Romero *et al*., 2015; Naets *et al*., 2022), benzoic acids (Camañes *et al*., 2015; Haile *et al*., 2017; Kumar *et al*., 2020), carbohydrates and oligosides (Agudelo-Romero *et al*., 2015; Camañes *et al*., 2015; Lacrampe *et al*., 2023), γ-aminobutyric acid (GABA) and the GABA shunt (Seifi *et al*., 2013; Naets *et al*., 2022; Lacrampe *et al*., 2023), and polyamines (Nambeesan *et al*., 2012; Agudelo-Romero *et al*., 2015; Lacrampe *et al*., 2023).

Discrepancies between studies could be explained by several factors linked to host genotype and organ specificity that fine-tune the metabolic response to infection along with variations in pathogen virulence or in timing and spatialization of defence (Kliebenstein *et al*., 2005; Mulema and Denby, 2012; Windram *et al*., 2012). The ability of pathogens, including necrotrophs, to subvert host immunity further complicates the interpretation of the response (Shao *et al*., 2021). Moreover, the intensity of the defence response, seen as the range of physiological processes that are regulated following infection, may be a poor indicator of resistance (i.e. the ability of the host to control fungal development). This has been shown for tomato fruits in which susceptibility factors expressed at ripening outweigh the strong immune response (Silva *et al*., 2021) or for tomato

stems where low N nutrition conferred high susceptibility despite large metabolic adaptations to infection (Lacrampe *et al.*, 2023). Thus, a better comprehension of the integrated metabolic adaptations of sink tissues that lead to effective resistance against necrotrophs is expected.

Metabolite concentrations, whose variations can reflect both synthesis and consumption, are complex to interpret. Metabolic fluxes, integrating levels of regulation from gene expression to reaction activities, allow a better analysis of the functional state of networks, to approximate the system-level behaviour of the organ under consideration (Yurkovich and Palsson, 2016). Direct measurement of metabolic fluxes by labelling experiments on whole organisms is complex and costly. An alternative lies in estimating fluxes by constraint-based models using growth data and metabolite contents to constrain a mathematical system defined by stoichiometric equations and the law of mass conservation (Williams *et al.*, 2010). By solving the system with optimality criteria characterized by an objective function, fluxes can be calculated at steady state (Sweetlove and Ratcliffe, 2011) as in flux balance analysis (FBA), a special case of the linear optimization method (Orth *et al.*, 2010). At the cell level, in contrast to kinetic models requiring a large number of parameters, constraint-based models require only the topology of the metabolic network (Clark *et al.*, 2020). Solving the model corresponds to calculating metabolic fluxes expected to best reflect the physiological state. First developed for unicellular systems, constraint-based models have now been developed (Sweetlove and Ratcliffe, 2011) and validated (Williams *et al.*, 2010) for plant cells and tissues. The complexity of metabolic networks due to metabolic diversity, redundancy of metabolic pathways, and subcellular compartments of specialized cells (Dersch *et al.*, 2016) limits the number of genome-scale metabolic models (GEMs) reconstructed from genomics annotations and requires manual curation (Collakova *et al.*, 2012). In the case of tomato, an original genome-scale model of leaves (Yuan *et al.*, 2016) was updated recently to model stems and roots (Gerlin *et al.*, 2022). A knowledge-based metabolic network of primary metabolism leading to a well-curated core model was relevant to describe the physiological behaviour of heterotrophic tissues, such as fruit, throughout development (Colombié *et al.*, 2017).

Regarding plant–pathogen metabolic modelling, few studies have been reported thus far. In the case of plants interacting with *Ralstonia solanacearum*, the costs of virulence factors were reported (Peyraud *et al.*, 2016). Cooperation within cells of the hyphae of *Sclerotinia sclerotiorum* colonizing *Arabidopsis thaliana* has been demonstrated by using FBA (Peyraud *et al.*, 2019). In tomato plants infected by the oomycete *Phytophthora infestans*, metabolic modelling helped in generating hypotheses about pathogen nutrition *in planta* (Rodenburg *et al.*, 2019). Here, to investigate the metabolic response of tomato stems infected by *B. cinerea,* a metabolic model was built to estimate metabolic fluxes and presumably identify key metabolic routes required for defence under variable N environments leading to contrasting susceptibilities. The model, constrained by a large metabolic dataset, was solved to calculate fluxes in symptomless stem tissues adjacent to inoculation points in *Botrytis*- and mock-inoculated plants. Metabolic fluxes and pathways supporting stem resistance or susceptibility against *B. cinerea* were examined.

Materials and methods

Plant material and inoculation of *B. cinerea*

The experimental set-up was previously reported in Lacrampe *et al.* (2021, 2023). Briefly, cv Clodano tomato plants were sown in a glasshouse on rockwool cubes and fertigated twice a day with a standard commercial nutrient solution (Liquoplant Rose, Plantin, Courthézon, France). Plantlets were transplanted 4 weeks after germination into 2 litre pots containing an inert mixture (1:1 v/v) of vermiculite and pozzolana. Seven weeks after germination, the fertigation solution was replaced by five nutrient solutions, corresponding to five experimental treatments, containing NO_3^- concentrations of 0.5, 2, 5, 10, or 20 mM and applied for an additional 4 weeks. In the solutions with reduced N concentrations, nitrates were substituted by sulfates to maintain the same electroconductivity in all treatments. All the other nutrients were maintained at the same concentration. Plants were watered according to the climatic demand, receiving the same amount of water regardless of the N supply level. A few hours before inoculation, the plants were transferred from the glasshouse to growth chambers, where an environment favourable to incubation was established (relative humidity 95%, temperature 21 °C, photosynthetic photon flux density 200 µmol m^{-2} s^{-1}). Inoculations were carried out by injecting a 10 µl aliquot of either a spore suspension (*Botrytis*-inoculated plants, strain BC1) or sterile water (mock-inoculated plants) on the petiole stub remaining after the excision of the sixth leaf of each plant. Fragments 2 cm long of the symptomless stem between the fifth and sixth internodes were sampled for analysis just before inoculation (0 days post-inoculation, dpi) and 2, 4, and 7 dpi. Two additional sets of stem samples were collected to measure dry matter content and growth (see below). As previously described, disease intensity was assessed at 4 dpi and 7 dpi by measuring lesion length along the stems. Fungal development decreased with increasing N supply (Lacrampe *et al.*, 2021, 2023), confirming previous results from similar experimental designs (Lecompte *et al.*, 2017).

Metabolite quantification and biomass composition

A total of 175 samples, corresponding to five biological replicates under five N supply levels and four time points (0, 2, 4, and 7 dpi) of mock- and *Botrytis*-inoculated plants, were analysed for soluble carbohydrates and polyols, organic acids, free amino acids, polyamines, phenolic compounds, glycoalkaloids, antioxidants, starch, proteins, cell wall, lipids, and nucleic acids. The analytic methods are summarized in Supplementary Table S1 and described in Lacrampe *et al.* (2023). Absolute quantification was obtained from the semi-quantitative data described in Lacrampe *et al.* (2023), using for each metabolite external calibration curves centred on the samples. The methods used for additional compounds not described in the previous study (lipids, glutathione, nucleic acids, and cell wall constituents) are presented hereafter.

Lipids were extracted from 20 mg of fresh powder for 90 min at 90 °C under constant stirring, with 475 µl of MeOH containing 68.4 µM heptadecanoic acid as an internal standard and 25 µl of H_2SO_4. Then, 500 µl of 2.5% NaCl and 650 µl of hexane were successively added, and the samples were incubated under stirring for 20 min at 90 °C. Samples were fast-centrifuged to speed the phase separation, and the upper phase containing hexane was collected and stored at –20 °C until analysis.

Quantification was performed using a 7890B GC System (Agilent Technologies, Santa Clara, CA, USA) equipped with a MultiPurpose Sampler (Gerstel GmbH & Co, Mülheim, Germany), split/splitless injector, Zebron ZB-SemiVolatiles 34.590 m×0.25 mm×0.25 µm column (Phenomenex, Torrance, CA, USA), and a Pegasus BT TOF mass spectrometer (LECO, St. Joseph, MI, USA). The MultiPurpose Sampler was controlled by Maestro Version 1.4.40.1 Gerstel, and the gas chromatography system with the mass spectrometer was controlled by ChromaTOF Version 5.20.38.0.54864 (LECO). A 1 µl aliquot of the sample was injected in splitless mode at 270 °C. Helium was used as the carrier gas at 1.0 ml min^{-1}. The initial oven temperature was kept at 70 °C for 1 min and then increased to 220 °C at a rate of 9 °C min^{-1}, increased again to 330 °C at a rate of 15 °C min^{-1}, and maintained for 5 min. The m/z scan range was 50–630 with a cycle time of 10 scans s^{-1} and an acquisition delay of 310 s. The source temperature and transfer line were set at 250 °C. Absolute quantification was performed using external calibration curves centred on the samples for each fatty acid methyl ester.

Total glutathione was quantified as the glutathione disulfide equivalent (Massot *et al*., 2013), thus the maximum amount of the reduced form (GSH) was defined as twice the maximum amount of the oxidized form (GSSG), as GSSG is a dimer of GSH molecules joined by a disulfide bridge (Meister and Anderson, 1983).

The basic cell wall constituents (uronic acids, carbohydrates, and lignins) were determined with a pool of samples as described in Renard *et al*. (1990).

RNA was isolated from 200 mg of frozen stem powder using the commercial RNeasy Plant Mini Kit (Qiagen, Hilden, Germany) following the manufacturer's instructions. Total RNA was quantified by measuring absorbance at 260 nm using a Nanodrop spectrophotometer.

Nitrates were estimated from five experiments carried out between 2009 and 2011 on equivalent experimental set-ups and several tomato genotypes (Abro *et al*., 2014).

The quantitative values obtained (in µmol) were first expressed in mass concentration (µmol g DW^{-1}) and then, in order to be used in the model, they were multiplied by the dry mass of 1 cm of stem (µmol cm^{-1} of stem, see below).

The full dataset of metabolite contents and biomass composition is provided in Supplementary Table S2.

Stem dry mass and growth measurement

Two additional sets of five stem fragments of 1 cm length (per treatment and sampling time) were sampled on each side of those taken for biochemical analyses and used to determine the dry matter content of stems as well as stem dimensions. Dry weight was measured 5 d after oven drying at 70 °C. On the other pool, fresh masses, lengths, and diameters of segments were assessed on photographs of samples frozen at the time of sampling. Pictures taken from a fixed-distance camera above the stem were analysed with ImageJ software (Version 1.52). Sample volumes and masses per unit length were deduced from the metrics (Supplementary Table S3).

The relative growth rate (RGR in d^{-1}) was calculated as the difference in mass per unit length between 0 dpi and 7 dpi divided by time and then by mass at 0 dpi. Samples dedicated to growth measurements under 10 mM NO_3^-, mentioned in a previous report (Lacrampe *et al*., 2023), were degraded during processing for growth measurements and not further considered, leaving four N treatments for modelling (i.e. 140 samples).

Flux balance model

The flux balance model was built, assuming non-compartmented stem cell tissue, according to the known stoichiometry of physiological reactions. Measured external compounds served as forcing constraints. Fifty-eight reactions, out of a total of 302 reactions in the model, were set as external, covering overall biomass components (cell wall, proteins, nucleic acids, lipids, and starch) and accumulated metabolites (free amino acids, carbohydrates, organic acids, redox compounds, and secondary metabolites). A previous model of heterotrophic plant central metabolism designed for tomato fruit (Colombié *et al*., 2015) was improved and extended using the Kyoto Encyclopedia of Genes and Genomes (KEGG; https://www.genome.jp/kegg/pathway.html) and PlantCyc (https://plantcyc.org/) databases to include additional reactions related to energetic cofactors, protein synthesis, nucleic acid synthesis, lignin synthesis, and pathways for the main secondary metabolites found after challenge by *B. cinerea*: the polyamines putrescine and spermidine; the phenolic compounds chlorogenic acid and rutin; and the glycoalkaloid α-tomatine (Supplementary Protocol S1). The synthesis and degradation of the main cofactors [folate, NAD(P), FAD, and CoA] were implemented. All these cofactors, in addition to ATP and ADP, were set as internal metabolites, which means that they were balanced in the model. NADPH is used for biosynthesis, while NADH and $FADH_2$ are involved in respiration.

The overall network is detailed in Supplementary Fig. S1, and a complete list of metabolites and stoichiometric reactions is given in Supplementary Tables S4 and S5. In this model, carbon (C) input occurs via the uptake of sucrose (*suc_up*) and glutamine (*gln_up*), while N enters the metabolism via nitrate (*no3_up*) and glutamine (*gln_up*).

Resolution of the model

Steady state

The model describes a set of n reactions involving m metabolites, of which m_{int} are internal metabolites. At steady state, the mass balance equation is expressed as follows:

$$\frac{dX_{int}}{dt} = N\ V = 0\ \#1$$

where X_{int} is the vector of m_{int} internal metabolites (m_{int}=177), V is the flux vector composed of the rates of n reactions of the network (n=302), and N is the stoichiometry matrix.

Constraints limiting the flux space

To solve the system and reduce the solution space, a lower and an upper bound constrained each flux (Supplementary Table S6). For internal reactions, thermodynamic properties were provided to set reversibility or irreversibility. Among 252 internal reactions, 179 were considered irreversible, which means that their lower bounds were set to zero.

Constraints relative to daily external fluxes were fitted from measured metabolite and biomass compound concentrations (in µmol cm^{-1}) at each time step. A monotone Hermite spline interpolation (Fritsch and Carlson, 1980) was used to fit data (illustrated for fructose in Supplementary Fig. S2C) from only three time points, in order to mitigate noise in spline interpolations: 0 dpi; 3 dpi as the average of observations at 2 dpi and 4 dpi; and 7 dpi. The spline parameters were then applied for each day accordingly. A linear regression throughout the time series was applied to the most abundant biomass components: cell wall, starch, and proteins (illustrated for proteins in Supplementary Fig. S2B). Standard deviations on regression residues are provided in Supplementary Table S7. The corresponding fluxes were determined by the first derivatives of the fitted functions and entered as lower and upper bounds to constrain the solution space of the model (Supplementary Table S6).

The flux of nucleic acids (*Vnucleo*) was determined from total RNA assays. The flux of diacyl-glycerol (*Vdag_ac*) was determined from the sum of quantified fatty acids. In addition, to match reported knowledge on tissue transcriptional activity, flux through phosphoenolpyruvate carboxykinase (*Vpepck*) was constrained by a maximum of 0.001 µmol g

DW^{-1} d^{-1}, as PEPCK transcripts were shown to be low in tomato stems (Bahrami *et al.*, 2001). The flux through the PPi-dependent phosphofructokinase (*Vpfp*) was also constrained by a maximum of 0.001 µmol g DW^{-1} d^{-1} to promote the flux through the ATP-dependent phosphofructokinase (*Vpfk*; PPi being set as an external compound, the model was forced to mobilize ATP through PFK).

Objective function

Minimization of the sum of squares of fluxes, which leads to a unique optimization solution for each condition (Holzhütter, 2006), was used as the objective function to solve the system and calculate fluxes each day from 1 dpi to 6 dpi (Supplementary Table S8). Finally, 48 flux solution vectors were obtained, calculated in µmol cm^{-1} d^{-1}, and converted on a dry weight basis (µmol g DW^{-1} d^{-1}) to compare conditions.

Software

The stoichiometric model (in sbml format, Supplementary Protocol S2) and mathematical problems were implemented with MATLAB (Mathworks R2023a, Version 9.14.0.2239454, Natick, MA, USA) and the optimization toolbox solver quadprog with an interior-point-convex algorithm for minimization. Prior to resolution, an analysis of the model architecture was performed using Metatool software Version 4.3 (Pfeiffer *et al.*, 1999). All data treatments and statistics were computed with R software (Version 4.2.1). Principal component analysis (PCA) was performed on cube-root-transformed and Pareto-scaled unbounded fluxes to approximate normal distribution using the NIPALS algorithm of the ropls package (Thévenot *et al.*, 2015). Hierarchical classification analysis (HCA) was performed on fluxes >0.001 µmol g DW^{-1} d^{-1} in absolute value in *Botrytis*- and mock-inoculated plants separately using Euclidean distance and the Ward algorithm. Spearman's correlation matrices were computed on fluxes >0.001 µmol g DW^{-1} d^{-1} in absolute value in *Botrytis*-inoculated plants and mock-inoculated plants separately, using combined data from all N supplies and all dpi. Flux maps were drawn with Cytoscape (Version 3.10.1).

Results

Infection by *B. cinerea* triggered local radial stem growth

Disease development, showing a curvilinear decrease in stem lesion size with increasing N supply, was described earlier (Lacrampe *et al.*, 2021, 2023) and is presented in Supplementary Fig. S3. The system considered for flux modelling was a unit length (in cm) of stem, located at least three nodes below the apex. Stem growth, away from the apex, was considered one-dimensional and radial. The RGR was thus measured from diameter and tissue density variations on stem fragments adjacent to the inoculation sites. A radial growth of mock-inoculated plants was observed, with RGR increasing with N supply from 0.011 d^{-1} to 0.027 d^{-1} (Fig. 1A). Surprisingly, the RGR of the *Botrytis*-inoculated plants was higher, ~0.03 d^{-1} for all treatments, and the difference from the mock-inoculated plants fading progressively with increased N supply. This was mostly the consequence of larger stem diameters achieved in the *Botrytis*-inoculated plants (Table 1), but also of an increase in dry matter content of *Botrytis*-inoculated plants under 0.5 mM NO_3^-. As a result, 7 dpi, the average dry weight per unit length of *Botrytis*-inoculated stems was 17.2, 8.7, 7.7, and 0.7% higher than that of mock-inoculated stems at 0.5, 2, 5, and 20 mM NO_3^-, respectively, leading to the RGR differences shown.

To achieve credible flux simulations, we first checked the mass conservation assumption by calculating the cumulative dry mass contents of biomass components and accumulated metabolites. High coverage was obtained, with ~90% of stem biomass quantified (Fig. 1B). The coverage decreased slightly under a high N supply, probably due to unmeasured compounds such as ions, notably potassium, which might account for 5–7% of the total biomass and accumulate more under a high N supply (Kirkby and Knight, 1977). The cell wall accounted for ~60% of the total biomass, and starch, sugars, free amino acids, and proteins together accounted for 30%. The proportion of amino acids and proteins increased with N supply, along with a decrease in starch and sugar contents.

The flux hierarchy was consistent with the activity of heterotrophic stem tissue

Model resolution led to 48 flux vectors, calculated for 6 dpi, under four different N supply and two inoculation conditions (Supplementary Table S8). A monotone Hermite spline interpolation (Fritsch and Carlson, 1980) was used to calculate the dry mass of samples at intermediate time points 1, 3, 5, and 6 dpi according to assessments at 0, 2, 4, and 7 dpi (Supplementary Fig. S2A). For each condition, the 302 fluxes varied by several orders of magnitude: 9–32 simulated fluxes, depending on the treatment, were >50 µmol g DW^{-1} d^{-1}, while nearly half were estimated to be <0.01 µmol g DW^{-1} d^{-1}. With the aim of first illustrating the general behaviour of the model regardless of nitrogen or infection, and this hierarchy between fluxes, the flux distribution for mock-inoculated plants grown under 5 mM NO_3^- is shown in Fig. 2—this treatment being chosen as an example. The most important fluxes were, as expected, associated with respiration (*Vco2_dis*=195 µmol g DW^{-1} d^{-1} in mock-inoculated plants under 5 mM NO_3^-), ATP generation from NADH (*Venergy1*=147 µmol g DW^{-1} d^{-1}) or $FADH_2$ (*Venergy2*=35 µmol g DW^{-1} d^{-1}), and central C metabolism. The sucrose uptake reaction—unconstrained—allowed C input associated with growth (*Vsuc_up*=102 µmol g DW^{-1} d^{-1}), while the flux for the other external source of C—glutamine—was lower and much more dependent on the treatment applied (Supplementary Fig. S4). The model predicted a cleavage of sucrose where the flux through sucrose synthase (*Vsusy*=83 µmol g DW^{-1} d^{-1}) dominated that through invertase (*Vinv*=19 µmol g DW^{-1} d^{-1}). This is probably the consequence of a high flux for the generation of cell wall components, notably from the SUSY-forming UDP-glucose (*Vcws*=110 µmol g DW^{-1} d^{-1}). Accordingly, flux through fructokinase (*Vfk*=101 µmol g DW^{-1} d^{-1}) was higher than that through hexokinase (*Vhk*=16 µmol g DW^{-1} d^{-1}). More surprising was the dominance of the oxidative pentose-phosphate pathway over glycolysis, with very high fluxes through glucose-6-phosphate

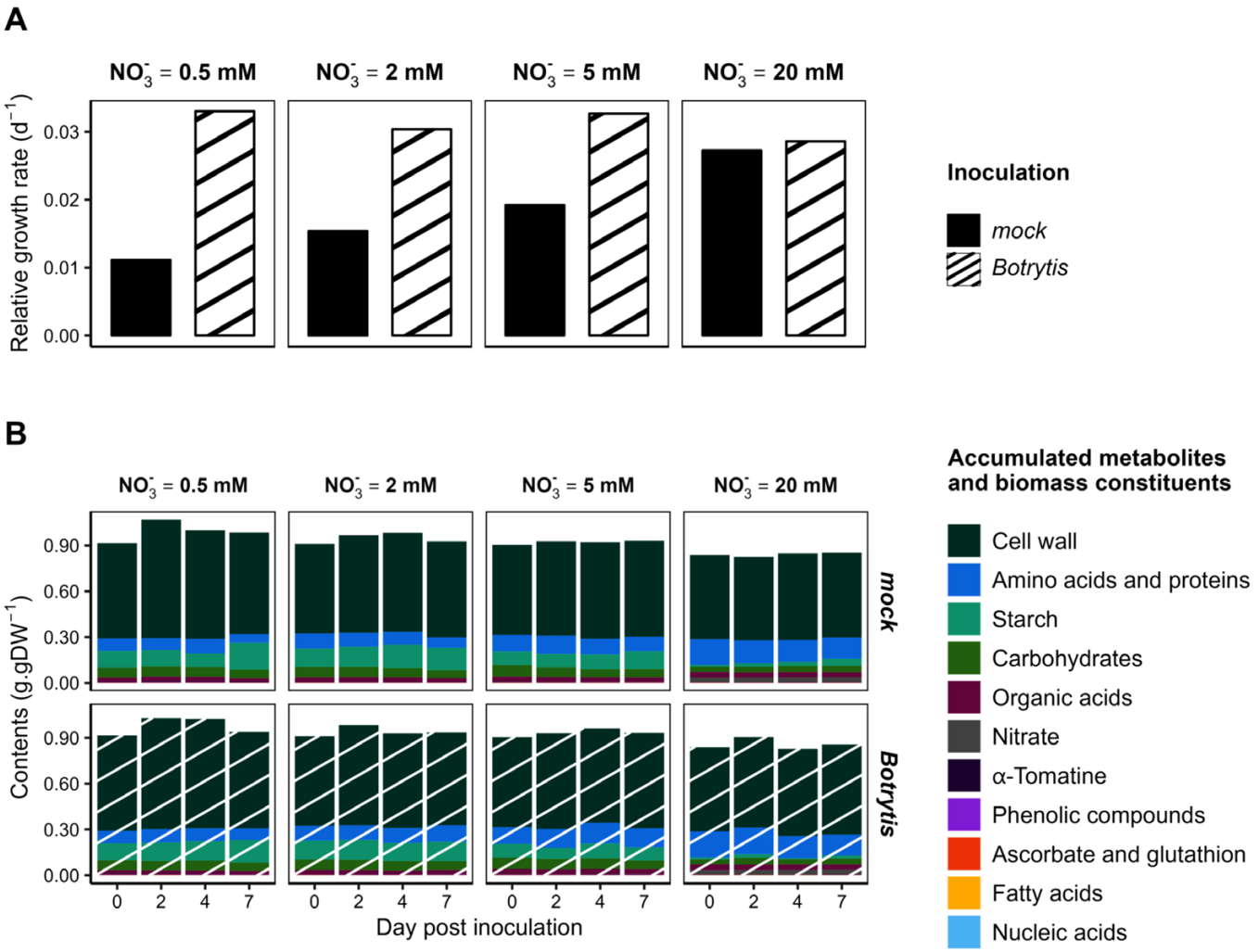

Fig. 1. Evolution and distribution of tomato stem biomass. (A) Relative growth rate (RGR; expressed in d^{-1}) of 1 cm long symptomless stem fragments of tomato plants grown under four levels of N supply (0.5, 2, 5, and 20 mM NO_3^-) and mock inoculated (black) or inoculated with *Botrytis cinerea* (striped white). (B) Mass balance of symptomless stems of tomato plants grown under four levels of N supply (0.5, 2, 5, and 20 mM NO_3^-) inoculated with mock or *B. cinerea*. Accumulated metabolites and biomass components are expressed in g g DW^{-1}. Each value corresponds to the mean of five biological replicates.

Table 1. Tomato stem diameters (cm)

	0.5 mM NO_3^-	2 mM NO_3^-	5 mM NO_3^-	20 mM NO_3^-
Mock-inoculated plants[a]	0.72 ± 0.06	0.92 ± 0.07	1.16 ± 0.06	1.20 ± 0.07
Botrytis-inoculated plants[a]	0.76 ± 0.06	0.98 ± 0.06	1.19 ± 0.07	1.19 ± 0.07
P-value[b]	0.0698	0.0074	0.2912	0.6529

[a] Values correspond to the mean of stem diameters (in cm) measured on all sampling days ±SD.
[b] *P*-value from a Wilcoxon–Mann–Whitney test comparing stem diameters of mock- and *Botrytis*-inoculated plants.

isomerase (*Vpgi*=127 µmol g DW^{-1} d^{-1}) and glucose-6-phosphate dehydrogenase (*Vg6pdh*=107 µmol g DW^{-1} d^{-1}). This was associated with a flux through Rubisco (*Vrbccar*=50 µmol g DW^{-1} d^{-1}), which generates 3-phosphoglycerate. Although the objective function minimized flux cycling, a surprising cycle was calculated between dihydroxyacetone-phosphate and glycerol-3-phosphate (*Vg3pdh1* and *Vg3pdh2*=25 µmol g DW^{-1} d^{-1}), probably to balance the reducing power. Finally, the TCA was predicted to function in a non-cyclic mode. In summary, the hierarchy between the fluxes calculated by the model reflected the functioning of a heterotrophic cell, in which disturbances by a necrotrophic infection do not modify the order of magnitude presented. Nevertheless, many fluxes were modified by infection, as shown below.

Fluxes were increased in infected susceptible plants

To evaluate the consequence of inoculation under each N supply, fluxes in *Botrytis*-inoculated plants were plotted against those of mock-inoculated plants (Fig. 3). Interestingly, fluxes

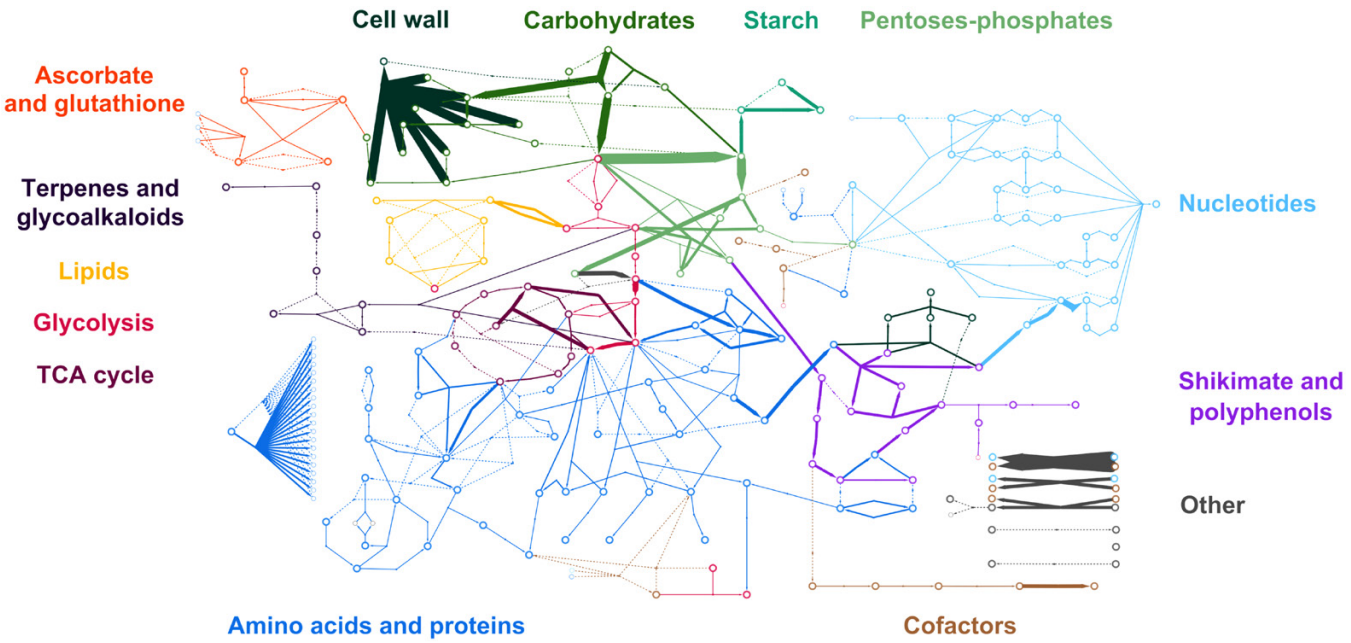

Fig. 2. Overall flux distribution. Flux maps of symptomless stems of mock-inoculated tomato plants grown under 5 mM NO_3^- 6 d post-inoculation. The open circles represent metabolites, and the sizes of the arrows represent the metabolic fluxes expressed in μmol g DW^{-1} d^{-1}. The dotted lines represent metabolic fluxes with an absolute value of <0.001 μmol g DW^{-1} d^{-1}. Each colour indicates a pathway. The complete network with all the names of the metabolites and reactions is presented in Supplementary Fig. S1.

in *Botrytis*-inoculated plants were higher, with the difference being greater under the lowest N supply rate, while fluxes in *Botrytis*- and mock-inoculated plants were comparable under the highest N supply level (20 mM NO_3^-). These higher fluxes were consistent with the above-mentioned increased growth measured in *Botrytis*-inoculated plants. Irrespective of day-to-day variations, the variation in C influx in the *Botrytis*-inoculated plants relative to the mock-inoculated plants was +40%, +18%, +29%, and –5% under 0.5, 2, 5, and 20 mM NO_3^-, respectively (Supplementary Fig. S4). Regarding high N supply (20 mM NO_3^-), the same RGR between *Botrytis*- and mock-inoculated plants, in addition to only weak differences in biomass composition and metabolite contents (Fig. 1), resulted in equivalent C influx and low differences in fluxes for most metabolic reactions.

Nitrogen influx was constrained by known nitrate stem contents but unconstrained by glutamine influx (Supplementary Fig. S4B). In mock-inoculated plants, except under 20 mM NO_3^-, basal metabolism relied upon N remobilization from proteins and most free amino acids. Remobilization might have been a consequence of the transition to a low-light environment in the growth chambers used for incubating *Botrytis*- and mock-inoculated plants, as plants grown temporarily in the dark are known to reduce their protein content (Weaver and Amasino, 2001). However, conversely, in *Botrytis*-inoculated plants, simulated glutamine uptake accounted for a large part of the N influx. Under a high N supply (20 mM NO_3^-), in both mock- and *Botrytis*-inoculated plants, available nitrates accounted for a significant part of the N influx.

The effects of inoculation and N supply were studied with a PCA performed on cube-root-transformed and Pareto-scaled unbounded fluxes of all 48 solution vectors of fluxes (Fig. 4). The first two principal components (PCs) explained 71% of the total variance. The first PC (57.8% of total variance) separated mock- from *Botrytis*-inoculated plants, and the second PC (12.7% of total variance) separated N supply levels, while the effects related to flux kinetics throughout the 6 dpi appeared minor (Fig. 4A). There was a smaller distance between mock- and *Botrytis*-inoculated plants under 20 mM NO_3^- in comparison with other N supply levels. The corresponding loading plot (Fig. 4B) allowed us to identify the main reactions supporting these results. Infection coincided with an opposite position along PC 1 for protein synthesis in *Botrytis*-inoculated plants (*prots*) compared with protein catabolism in mock-inoculated plants (*protd*), amino acid metabolism (*bcaat1*, *bcaat2*, *bcaat3*, *aspat*, and *p5cs*), nitrogen metabolism (*gln_up*, *gogat*, *gs*, and *n_dis*) and part of TCA cycle reactions (*idh*, *aco*, and *cs*), while the effect of N supply relied on reactions associated with sugar assimilation (*hk* and *inv*), glycolysis (*pfk*, *ald*, *tpi*, *gapgh*, and *pgk*), starch synthesis (*pgm*, *agpase*, and *ss*), terpene synthesis (*mepp*, *dmat*, and *ipdpi*), and citramalate (*citmaldh* and *citmals*). In summary, in agreement with the observed radial growth under N supplies lower than 20 mM NO_3^-, higher fluxes were estimated for

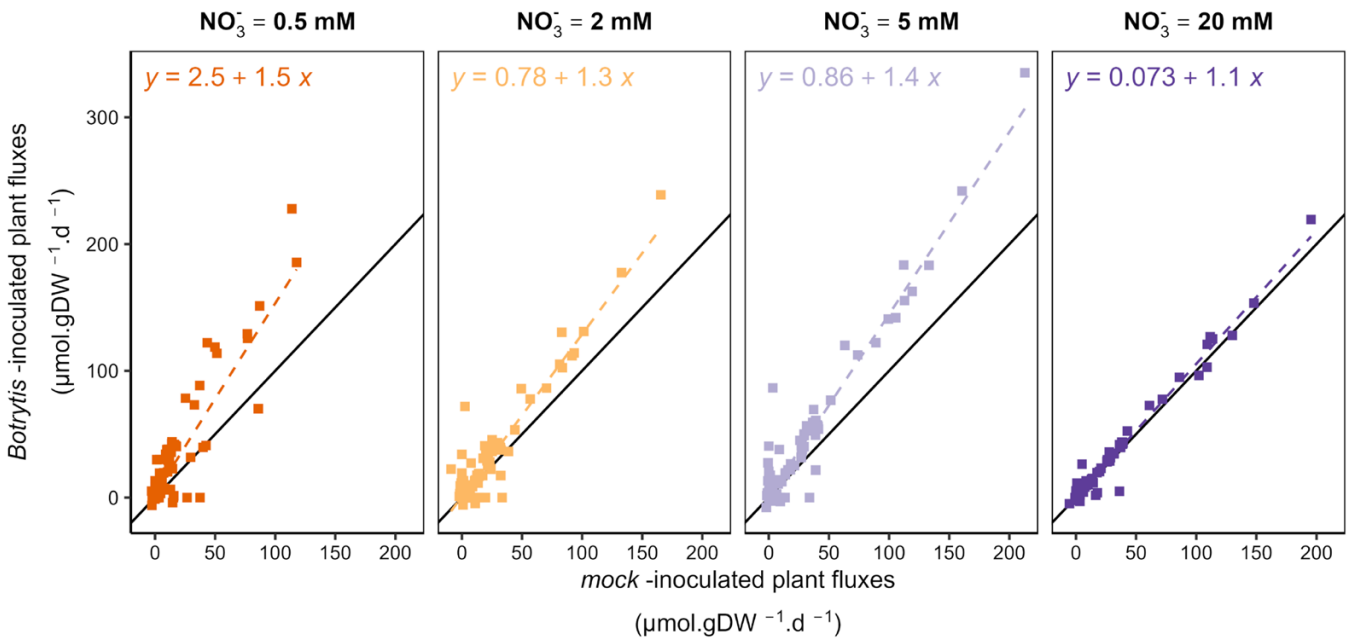

Fig. 3. Impact of inoculation on flux distribution. Averaged fluxes (in µmol g DW^{-1} d^{-1}) over the 6 d post-inoculation of *Botrytis*-inoculated plants versus those of mock-inoculated plants under each N supply (0.5 mM NO_3^- in orange, 2 mM NO_3^- in yellow, 5 mM NO_3 in light purple, and 20 mM NO_3^- in dark purple). The dashed line represents the linear regression line associated with the equation, and the black line represents the identity line.

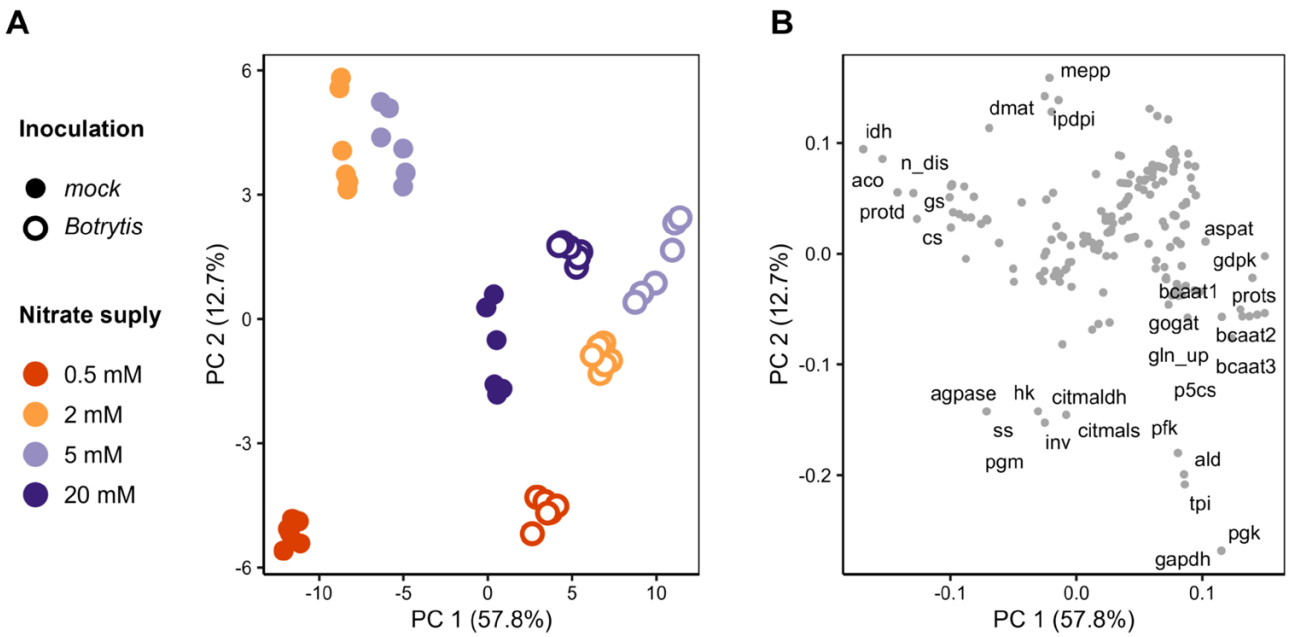

Fig. 4. Discrimination of fluxes according to both inoculation and N supply. Principal component analysis (PCA) performed on unbounded fluxes >0.001 µmol g DW^{-1} d^{-1} (in absolute value). Data were cube-root-transformed and Pareto-normalized (mean-centred and divided by the root-square of standard deviation). (A) Score plot with one point for each simulated condition. Filled circles, mock-inoculated plants; open circles, *Botrytis*-inoculated plants. N supply is represented by colour: 0.5 mM NO_3^- in orange, 2 mM NO_3^- in yellow, 5 mM NO_3^- in light purple, and 20 mM NO_3^- in dark purple. The simulation days are not differentiated. (B) Loading plot with the names of the 15 reactions contributing most to principal component (PC) 1 and PC 2.

Botrytis-inoculated plants than for mock-inoculated plants. In-depth profiles of pathways associated with metabolic changes were then examined.

In the metabolic model, some fluxes were correlated, for example fluxes of successive steps in a given metabolic pathway. Thus, the consequence of infection by *B. cinerea* can

be inspected by examining how the fluxes were correlated or decorrelated, using correlation matrices (Supplementary Tables S9, S10) and HCA to visualize the results from clusters of fluxes related to common pathways. The HCA of unbounded fluxes of *Botrytis*-inoculated plants revealed four main clusters (Fig. 5). These clusters differed from those of mock-inoculated plants (Supplementary Fig. S5). A few reactions are different in the two analyses because insignificant fluxes (<0.001 μmol gDW^{-1} d^{-1} in absolute value) were not accounted for in the HCA. The results of flux associations are illustrated in Figs 6 and 7 showing flux maps highlighting the clustering for *Botrytis*-inoculated plants and the time course of representative fluxes in the cluster (shown for *Botrytis*- and mock-inoculated plants).

Fluxes associated with cell wall synthesis increased with B. cinerea infection

Cluster 1.1.1 (Fig. 5) gathered reactions associated with cell wall synthesis, the pentose-phosphate pathway, the shikimate pathway, the production of monolignols and lignin, ATP synthesis, CO_2 dissipation, and the metabolism of some amino acids: serine, alanine, glycine, methionine, tyrosine, and phenylalanine (Fig. 6). The same cluster occurred in the HCA of mock-inoculated plants (in red in Supplementary Fig. S5). The fluxes through all these reactions were highly correlated, with Spearman's correlation coefficients exceeding 0.85 (Supplementary Tables S9, S10). Accordingly, the time course of fluxes (Fig. 6) displayed similar profiles with slight variations over time but higher fluxes, from two to three times in *Botrytis*-inoculated plants compared with mock-inoculated plants under low N supply (0.5, 2, and 5 mM NO_3^-). Thus, for the reactions in this cluster, in the case of low-susceptibility plants grown under 20 mM NO_3^-, the increase in fluxes following infection by the fungus was barely perceptible, whereas it was much more substantial in plants grown under lower N supplies, where the fungus has developed to a greater extent.

Fluxes through the TCA cycle and towards protein synthesis in Botrytis-inoculated plants were limited under very low N

Cluster 1.1.2 (Fig. 5) included protein synthesis, part of the TCA pathway, and reactions related to the metabolism of several amino acids: branched-chain amino acids (leucine, isoleucine, and valine), lysine, cysteine, aspartate, arginine, glutamate, ornithine, citrulline, and proline (Fig. 7). This cluster differed from others in two ways: (i) regardless of the N supply, the absolute value of fluxes was much higher in the *Botrytis*-inoculated plants than in the mock-inoculated plants, and (ii) for most reactions, the flux in the *Botrytis*-inoculated plants was lower under 0.5 mM and 20 mM NO_3^- than under 2 mM or 5 mM NO_3^-.

Proteins accumulated in *Botrytis*-inoculated plants and were degraded in mock-inoculated plants. Consequently, the flux of protein synthesis (*Vprots*) was positive in the *Botrytis*-inoculated plants and null in the mock-inoculated plants, whereas the flux of protein degradation (*Vprotd*) was null in the *Botrytis*-inoculated plants and positive in the mock-inoculated plants (Fig. 7). The total free amino acid content represented 5–15% (depending on N supply) of the mass of the proteins in the total biomass, and their concentrations remained stable or even increased in *Botrytis*-inoculated plants, with moderate depletion only noted for asparagine, glutamine, and glycine

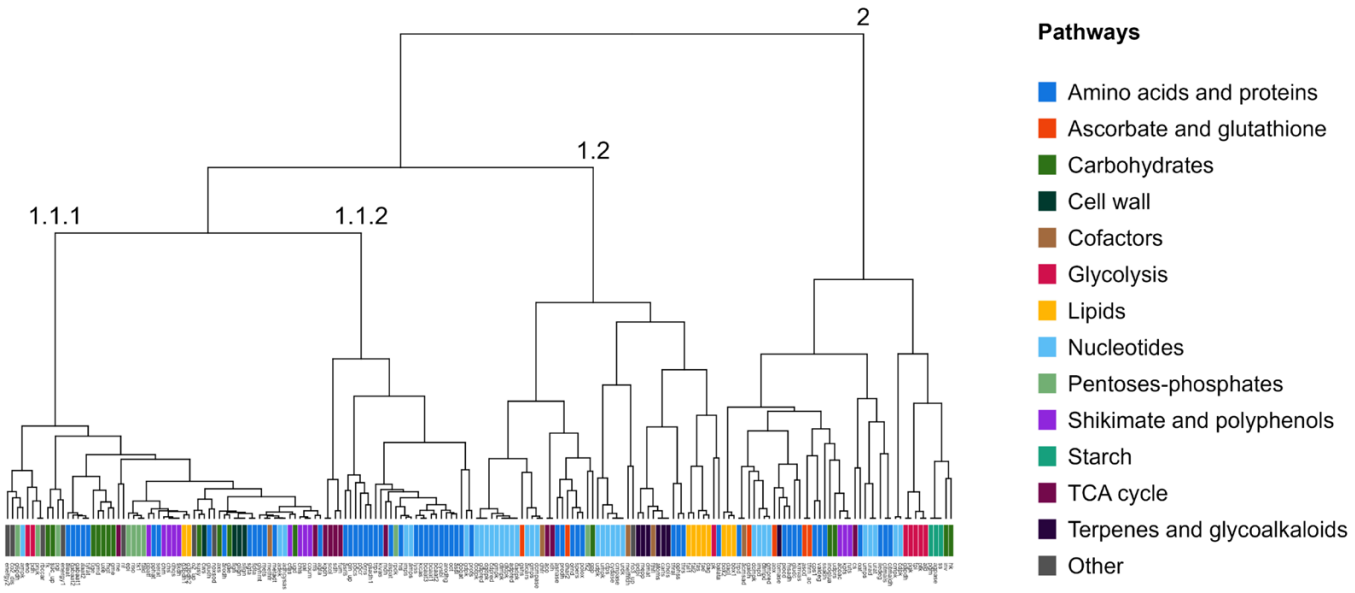

Fig. 5. Coordination within the metabolic network of *Botrytis*-inoculated plants. Hierarchical clustering analysis (HCA) performed on unbounded fluxes >0.001 μmol g DW^{-1} d^{-1} (in absolute value) of *Botrytis*-inoculated plants. Data were cube-root-transformed and Pareto-normalized (mean-centred and divided by the root-square of standard deviation). HCA was performed using the Euclidean distance and the Ward algorithm. Each reaction was coloured according to metabolic pathways.

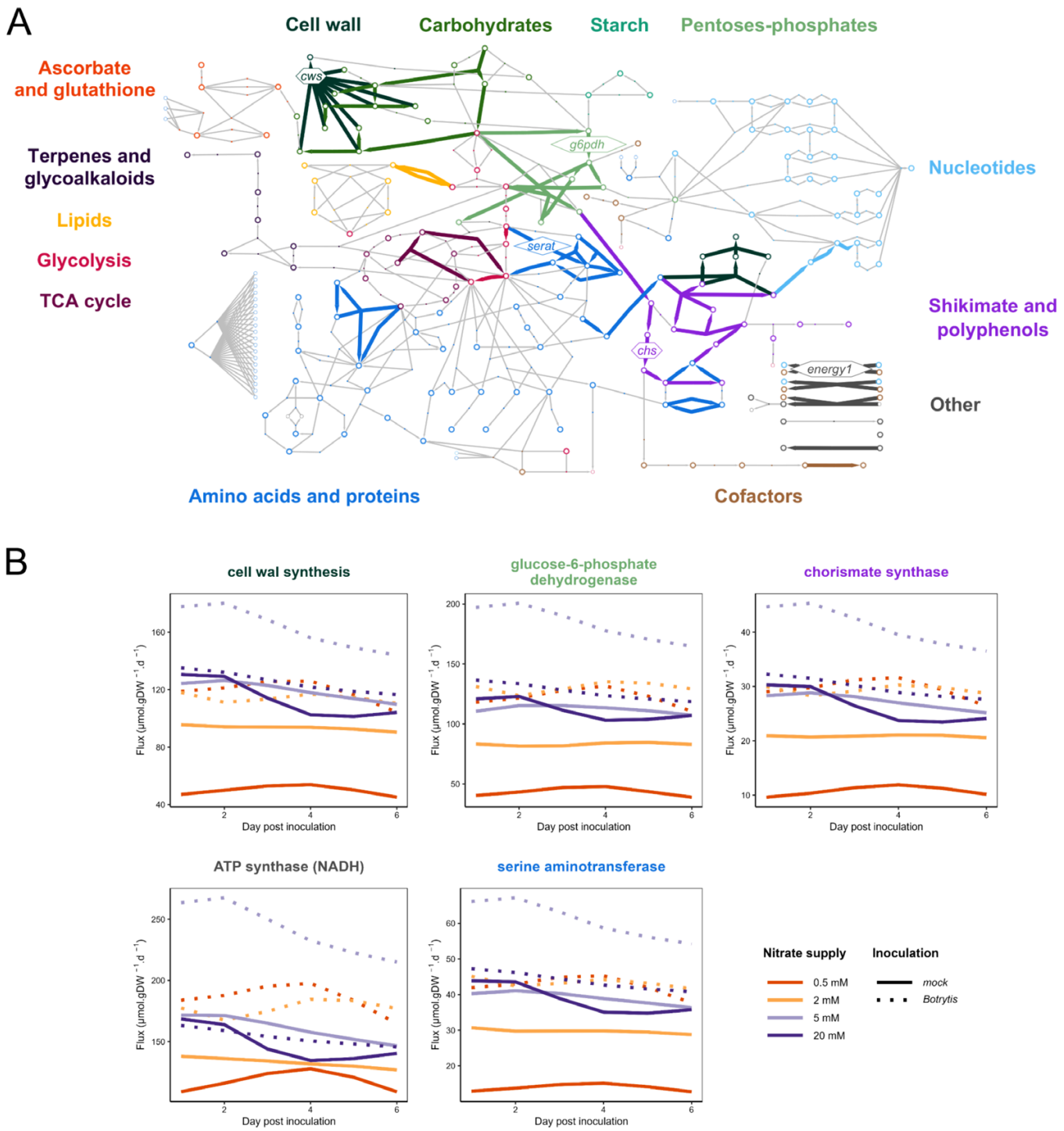

Fig. 6. Cell wall synthesis-associated reactions in *Botrytis*-inoculated plants. (A) Simplified metabolic network highlighting reactions from HCA-derived Cluster 1.1.1 of unbounded fluxes >0.001 µmol g DW^{-1} d^{-1} (in absolute value) of *Botrytis*-inoculated plants (see Fig. 5). The open circles represent metabolites, the arrows highlight the reactions contained in the cluster, and the lines represent the other reactions of the network. Each colour refers to a pathway. The reactions shown, in hexagons for irreversible reactions and in diamonds for reversible reactions, correspond to those whose fluxes are illustrated in (B): *cws*, cell wall synthesis; *g6pdh*, glucose-6-phosphate dehydrogenase; *chs*, chorismate synthase; *energy1*, ATP synthase NADH dependent; *serat*, serine aminotransferase. The complete network with all the names of the metabolites and reactions is presented in Supplementary Fig. S1. (B) Time course of the five most representative fluxes of the cluster. Fluxes of symptomless stems of tomato plants grown under four levels of N supply (0.5 mM NO_3^- in orange, 2 mM NO_3^- in yellow, 5 mM NO_3^- in light purple, and 20 mM NO_3^- in dark purple) and mock inoculated (solid lines) or inoculated with *B. cinerea* (dashed lines) were expressed in µmol g DW^{-1} d^{-1}.

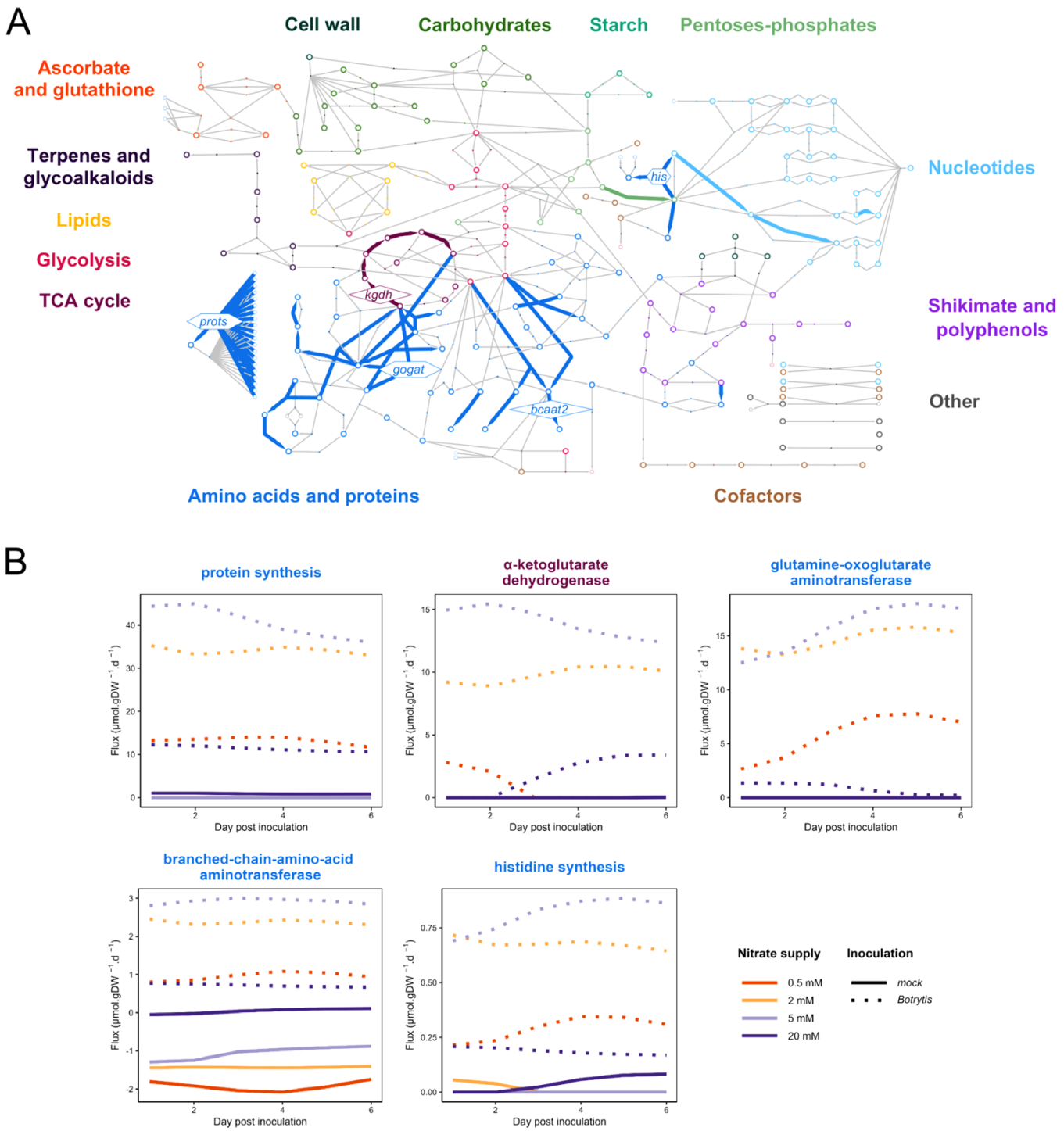

Fig. 7. Protein synthesis-associated reactions in *Botrytis*-inoculated plants. (A) Simplified metabolic network highlighting reactions from HCA-derived Cluster 1.1.2 of unbounded fluxes >0.001 µmol g DW^{-1} d^{-1} (in absolute value) of *Botrytis*-inoculated plants (see Fig. 5). The open circles represent metabolites, the arrows highlight the reactions contained in the cluster, and the lines represent the other reactions of the network. Each colour refers to a pathway. The reactions shown, in hexagons for irreversible reactions and in diamonds for reversible reactions, correspond to those whose fluxes are illustrated in (B): *prots*, protein synthesis; *kgdh*, α-ketoglutarate dehydrogenase; *gogat*, glutamine-oxoglutarate aminotransferase; *bcaat2*, branched-chain amino acid aminotransferase; *his*, histidine synthesis. The complete network with all the names of the metabolites and reactions is presented in Supplementary Fig. S1. (B) Time course of the five most representative fluxes of the cluster. Fluxes of symptomless stems of tomato plants grown under four levels of N supply (0.5 mM NO_3^- in orange, 2 mM NO_3^- in yellow, 5 mM NO_3^- in light purple, and 20 mM NO_3^- in dark purple) and mock inoculated (solid lines) or inoculated with *B. cinerea* (dashed lines) were expressed in µmol g DW^{-1} d^{-1}.

(Supplementary Table S2). Thus, protein synthesis in *Botrytis*-inoculated plants required *de novo* amino acid synthesis and turnover. Accordingly, the fluxes through amino acid synthesis, in particular those derived from ribose-5-phosphate, pyruvate, and α-ketoglutarate, were increased in the *Botrytis*-inoculated plants (Fig. 7, *Vgogat*, *Vbcaat2*, and *Vhis*). Interestingly, the fluxes in the TCA cycle linking α-ketoglutarate to oxaloacetate through succinate were also high (*Vkgdh*, *Vscol*, *Vsdh*, *Vfum*, and *Vmdh*), but there was no synthesis of α-ketoglutarate from citrate in *Botrytis*-inoculated plants (*Vaco* and *Vidh*). Thus, the synthesis of glutamate and α-ketoglutarate relied on glutamine import and regeneration from other amino acid metabolic routes. Indeed, 65–77% of the flux through α-ketoglutarate synthesis in *Botrytis*-inoculated plants (a total of 73–139 μmol g DW^{-1} d^{-1} depending on N supply) originated from serine (*Vserat*) and phenylalanine (*Vpphat*) transaminases.

This association of flux changes in the TCA cycle with increased amino acid and protein syntheses in *Botrytis*-inoculated plants is one interesting result of the model.

Lower fluxes towards starch synthesis were observed in Botrytis-inoculated plants

Cluster 2 (Fig. 5) gathered reactions leading to starch synthesis, with higher fluxes in mock-inoculated plants than in *Botrytis*-inoculated plants, regardless of the N supply level (Supplementary Fig. S6). These fluxes were correlated to those through invertase (*Vinv*) and hexokinase (*Vhk*, Supplementary Tables S9, S10). However, *Vinv* and *Vhk* fluxes were quite similar between mock- and *Botrytis*-inoculated plants, except under 20 mM NO_3^-. Additionally, under the three lowest N supply levels, glycolytic fluxes between fructose-6-phosphate and 3-phosphoglycerate (illustrated by 6-phosphofructokinase, *Vpfk*) were greatly increased in *Botrytis*-inoculated plants, especially at the end of the simulation period. This suggests that under these conditions, part of the flux through invertase was also directed towards glycolysis. The flux through citrate synthase (*Vcs*) was also represented in this cluster; it was high and decreased with N supply in mock-inoculated plants, while it was low or null in *Botrytis*-inoculated plants. There was, in mock-inoculated plants, a continuous flux in the TCA cycle between citrate and α-ketoglutarate, which was not observed in *Botrytis*-inoculated plants, where the flux was the other way round, regenerating citrate from α-ketoglutarate (see also Fig. 7). The flux through glutamate decarboxylase (*Vgludc*), directly guided by the constraints, was positive only up to 5 mM NO_3^- in mock-inoculated plants and was highly correlated with the dynamics of GABA accumulation or depletion (Supplementary Fig. S6; Supplementary Tables S9, S10).

Other fluxes varied according to time, inoculation, and N supply

Finally, the last cluster, Cluster 1.2 (Fig. 5), contained reactions from various metabolic pathways, including specialized metabolism and redox: MEP/DOXP (2-C-methyl-d-erythritol 4-phosphate/1-deoxy-d-xylulose 5-phosphate), terpenoids, fatty acids, nucleotides, antioxidants, and polyamines (Supplementary Fig. S7). The fluxes in this cluster varied with time, and differences between mock- and *Botrytis*-inoculated plants also varied depending on the N supply. Most of the reactions of this cluster were not decisive for the discrimination between mock- and *Botrytis*-inoculated plants or N supply achieved by PCA (Fig. 3B). However, some reactions showed interesting flux patterns. As mentioned above, the flux through aconitase (*Vaco*) and isocitrate dehydrogenase (*Vidh*), two TCA cycle reactions forming α-ketoglutarate from citrate, showed opposing directions depending on inoculation, regardless of the N supply (Supplementary Fig. S7). The flux through pyruvate kinase (*Vpk*, Supplementary Fig. S7), yielding pyruvate, increased with time in the *Botrytis*-inoculated plants and was higher than that in the mock-inoculated plants, except under 0.5 mM NO_3^-, where the flux was lower in the *Botrytis*-inoculated plants until 3 dpi. This low flux under very low N (0.5 mM NO_3^-) resembled those observed for the TCA cycle and some amino acid and protein synthesis, and might suggest several points of regulation by N of defence-related metabolism activation, starting in glycolysis. Additionally, *Vpk* was strongly correlated with the flux through malate dehydrogenase (*Vmdh*) in *Botrytis*-inoculated plants only. The total flux of pyruvate production was 1–3 times higher in the *Botrytis*-inoculated plants than in the mock-inoculated plants. The flux through enzymes that synthetize glutathione from glutamate, cysteine, and glycine (*Vgshs*) was much higher in *Botrytis*-inoculated plants under N supplies of 2, 5, and 20 mM NO_3^-, with the maximum reached on different days after inoculation (Supplementary Fig. S7). Moreover, the model simulated a quasinull flux through the mevalonate pathway, while the flux through the MEP/DOXP pathway was significant. This flux was correlated with α-tomatine accumulation in *Botrytis*-inoculated plants only (Supplementary Tables S9, S10); however, there was no clear trend for the effect of inoculation on α-tomatine accumulation or degradation.

Discussion

N-dependent host defence and susceptibility to *B. cinerea*

In the present study, metabolic fluxes in primary and secondary metabolic pathways of tomato stems were calculated based on a large dataset acquired from 140 biological samples (five biological replicates, four different N supplies, and four time points for mock- and *Botrytis*-inoculated plants) covering most of the biomass composition. The analysis focused on symptomless stem fragments adjacent to the growing lesions. Under the highest N supply (20 mM NO_3^-), very low disease propagation was accompanied by little metabolic adaptation, although variations in galactinol and alanine contents

indicated that the tissue perceived the infection (Lacrampe *et al.*, 2023). Accordingly, under 20 mM NO_3^-, the computed metabolic fluxes appeared relatively similar between the *Botrytis*- and mock-inoculated plants (Fig. 3), the difference consisting mainly of a reduced flux towards starch synthesis in the *Botrytis*-inoculated plants. It can be speculated that under a high N supply, strong pre-formed defences limit pathogen development since the time of infection, making it unnecessary for adjacent tissues to trigger additional defence mechanisms and strong metabolic adaptations. Additionally, in the chemical warfare between the pathogen and its host, little fungal development may limit host adaptation (Veloso and Van Kan, 2018). Conversely, when N was limiting, ≤5 mM NO_3^-, disease propagation increased, and profound metabolic changes were observed. A curvilinear response of tomato susceptibility to N supply has been repeatedly reported (Lecompte *et al.*, 2017), with susceptibility increasing steadily when diminishing the N supply below 10 mM NO_3^-. Similar evidence of high N resistance has also been observed on tomato leaves for different cultivars, but in several other species a high N supply stimulates *B. cinerea* development (Yermiyahu *et al.*, 2006; Lecompte *et al.*, 2013; Soulie *et al.*, 2020). Nitrogen, as a basal element of biological cells, interferes in many aspects of plant–pathogen interactions. Along with intervening in host defense, N shapes plant architecture and modifies the structure of susceptible tissues as well as the microclimate governing pathogen development. N-based compounds in the host also constitute resources for pathogens, and may modulate pathogen transcriptome and effector machinery in both biotrophic and necrotrophic interactions (Lanver *et al.*, 2018; Westrick *et al.*, 2019). It is therefore difficult to establish general rules for the effect of host nitrogen nutrition on pathogen susceptibility (Fagard *et al.*, 2014), the dependence on the N resources of living host tissues seeming, however, marked for biotrophic pathogens.

The high number of genes and quantitative trait loci (QTLs) associated with defence against and resistance to *B. cinerea* illustrate the complexity and polymorphism of plant defence. Despite this, strong markers of susceptibility or resistance have been shown at several omics levels. In tomato fruits, susceptibility factors have been associated with pectin degradation in the cell wall and with the expression of pathogen polygalacturonases (Silva *et al.*, 2023). Fructose content is a marker of resistance to *B. cinerea* in tomato stems and fruits (Lecompte *et al.*, 2017; Luna *et al.*, 2020). In these recent works and others, cell-level adaptations have suggested key metabolic functions involved in defence response: primary metabolism, cell wall strengthening, defence-oriented protein synthesis, and production of antifungal metabolites. In addition, various antimicrobial peptides and defence-related proteins are synthesized following *B. cinerea* infection, as illustrated by the high expression of genes encoding β-1,3-glucanases (Benito *et al.*, 1998; Rasul *et al.*, 2012), chitinases (Salzman *et al.*, 1998; Hatmi *et al.*, 2014; Silva *et al.*, 2021), protease inhibitors (Chassot *et al.*, 2007; Fan *et al.*, 2019), or defensins (Thomma *et al.*, 1998; Zheng *et al.*, 2006). This is consistent with the higher protein synthesis observed in *Botrytis*-inoculated plants in this study.

B. cinerea infection triggers stem growth and requires additional resources

As a consequence of unexpected radial growth, the RGRs of stem fragments adjacent to the lesions were increased in *Botrytis*-inoculated plants by 197% to 5% from 0.5 mM to 20 mM NO_3^- compared with mock-inoculated plants (Fig. 1A). This additional growth, observed on each series of independent samples corresponding to the different levels of nutrition (except 20 mM NO_3^- where it was barely perceptible), was strongly correlated with disease intensity. Although the physiological regulation behind this additional growth is not known, this finding suggests that tissues adjacent to fungal lesions received additional resources from distal tissues. Another indication of resource allocation towards growth was the reduced starch accumulation, regardless of the N supply, in *Botrytis*-inoculated plants (Supplementary Fig. S6). These results on starch metabolism confirm those of previous works (Rowe *et al.*, 2010; De Cremer *et al.*, 2013; Vega *et al.*, 2015; Badmi *et al.*, 2022). A local influx of resources associated with growth, which allows a shift of metabolism towards defence, is not incompatible with the general concept of the growth–defence trade-off. Chemical defence production to the detriment of growth or fitness has been widely observed at the whole-plant scale (Sestari and Campos, 2022). In our model, the additional resources directed to stem tissues close to the site infection might have been detrimental to the growth of other organs, source tissues, or fruits, and this requires further investigation. It has been suggested that 'endurance' mechanisms aiming at maintaining cell viability, via the production of energy to sustain the synthesis of antifungal compounds and antioxidants to limit ROS-induced cell death, are effective against necrotrophs (Seifi *et al.*, 2013; Tarkowski *et al.*, 2020). This could be achieved by recycling cell metabolites such as glutamate or GABA and/or by the supply of substrates from distal tissues. The latter hypothesis has received little experimental support thus far, and we provided evidence that C and N resources were imported in challenged tissues.

To match the increased growth observed in *Botrytis*-inoculated plants, the model suggested a more significant import of sucrose and glutamine, the main sources of C and N, respectively, in the phloem (Valle *et al.*, 1998; Ruan, 2014). The import of reduced N from glutamine was less energy consuming than the reduction of nitrates by nitrate and nitrite reductases and the incorporation of NH_4^+ via glutamine synthase. Accordingly, the model did not require flux of these enzymes in *Botrytis*-inoculated plants importing glutamine. This might be questionable, even in stem sink tissues that might not be very involved in N assimilation (Forde and Lea, 2007; The *et al.*, 2021). Moreover, it would require knowing where this

additional N, necessary for additional protein synthesis, came from, especially in conditions of very limited N supply. Nevertheless, the model coherently simulated less glutamine import under 0.5 mM NO_3^-, associated with the lowest fluxes towards protein synthesis, in comparison with less severe N-limiting supplies. As fluxes towards glutamate synthesis, mainly from glutamate dehydrogenase and GOGAT, and other amino acids via transaminases, were coherent, the absence of flux through glutamine synthase did not seem to affect the rest of the metabolic network.

Fluxes towards defence components

The quantified compounds, accumulated metabolites, and biomass components have a putative role in defence against *B. cinerea*. Did some of these compounds accumulate more than others, so that the distribution of biomass components was altered in *Botrytis*-inoculated plants in comparison with mock-inoculated plants? This situation was striking for proteins, for which the percentage in biomass composition increased in *Botrytis*-inoculated plants by 17, 29, and 23% under 0.5, 2, and 5 mM NO_3^-, respectively, while no difference was noticed under high N supply (20 mM NO_3^-). The accumulation of amino acids after pathogen infection can trigger responses, dependent or not on defence pathways (Zeier, 2013; Rojas *et al.*, 2014; Tarkowski *et al.*, 2020). Transcriptomic studies have highlighted the frequent up-regulation of amino acid metabolism after infection by *B. cinerea*, especially branched-chain and aromatic amino acids (Windram *et al.*, 2012; De Cremer *et al.*, 2013; Vega *et al.*, 2015; Kumar *et al.*, 2020; Xiao *et al.*, 2022). Accumulation or depletion of amino acids has been frequently reported, with large variations between studies (Hong *et al.*, 2012; Camañes *et al.*, 2015; Kumar *et al.*, 2020; Lacrampe *et al.*, 2023). However, measurements of metabolic contents may be poor indicators of compound turnover; thus, the higher fluxes found in this study in almost every amino acid pathway (Figs 6, 7) give a clear clue of their involvement in defence. Amino acids are precursors of several families of defence-oriented secondary metabolites. For instance, genes of the shikimate pathway forming aromatic amino acids from carbohydrates, as well as those encoding the enzyme phenylalanine-ammonia lyase (PAL), which catalyses the first committed step of the phenylpropanoid pathway, are up-regulated in several host plants following *B. cinerea* infection (Ferrari *et al.*, 2003; Rowe *et al.*, 2010; Agudelo-Romero *et al.*, 2015). It is interesting to note that exogenous applications of some amino acids or overexpression of amino acid biosynthetic pathways may enhance resistance to *B. cinerea* (Brauc *et al.*, 2012; Rasul *et al.*, 2012; Sun *et al.*, 2019; Oliva *et al.*, 2020). Here, considering that the amino acid and protein contents before inoculation were all higher as the N supply was high, it can be speculated that the limited increase in protein content under the lowest N supply level was insufficient for efficient defence. To examine this hypothesis further, a quantitative analysis of proteome evolution after infection would be necessary.

Additionally, significant increases in the distribution of rutin (as the major flavonoid) and glutathione in the biomass composition of *Botrytis*-inoculated plants suggest a multifaceted evolution of tissue metabolism for defence. The model predicted a very limited increased in fluxes towards glutathione metabolism under very low N supply, which might have contributed to increased susceptibility, as redox-mediated plant defence against *B. cinerea* has been frequently highlighted (Kuźniak and Skłodowska, 2005). Increased fluxes towards nucleotides and lipids were also limited under 0.5 mM NO_3^- compared with higher supply rates. This suggests that the effectiveness of the defence of tomato against *B. cinerea* depends on the activation of numerous metabolic pathways, and that severe nitrogen stress may prevent the activation of some of them. A summary diagram of the principal metabolic responses observed following infection is given in Fig. 8.

Unexpected crosstalk between glycolysis, the TCA cycle, and amino acid metabolism

Apart from generally increased fluxes in *Botrytis*-inoculated plants, the coordination inside the network was affected by the combination of infection and N supply. These changes were identified by examining flux correlation and clustering in the different conditions. Reactions towards starch synthesis, cell wall synthesis, monolignol synthesis (via the pentose-phosphate and shikimate pathways), and glycolysis between glucose-6-phosphate and 3-phophoglycerate resulted in similar correlations and clustering between fluxes of mock- and *Botrytis*-inoculated plants (Fig. 5; Supplementary Fig. S5). For this part of the network, the fluxes were simply translated following infection, irrespective of the N supply—except under 20 mM NO_3^-, where there was little increased flux in *Botrytis*-inoculated plants, as discussed earlier. Conversely, for a large part of the network, N supply modified the difference between fluxes in *Botrytis*- and mock-inoculated plants. In particular, fluxes in *Botrytis*-inoculated plants supplied with 0.5 mM NO_3^- showed limited increases in comparison with plants supplied with 2 mM or 5 mM NO_3^-. This notably occurred in the coordination of glycolysis, the TCA cycle, and amino acid metabolism: starting from pyruvate kinase, continuing in reactions of the TCA cycle between α-ketoglutarate and malate, up to the synthesis of several amino acids derived from oxaloacetate and α-ketoglutarate (ornithine, citrulline, arginine, lysine, isoleucine, leucine, valine, aspartic acid, asparagine, threonine, and histidine). Among this group of amino acids, arginine and branched-chain amino acids have already been identified as important determinants of the interaction between *B. cinerea* and its host plant (Brauc *et al.*, 2012; Windram *et al.*, 2012; Li *et al.*, 2021; Xiao *et al.*, 2022).

Conclusion

The examination, with constraint-based analysis, of tomato metabolic response to *B. cinerea* infection in stem source tissues proximal to the growing lesions indicated boosted fluxes

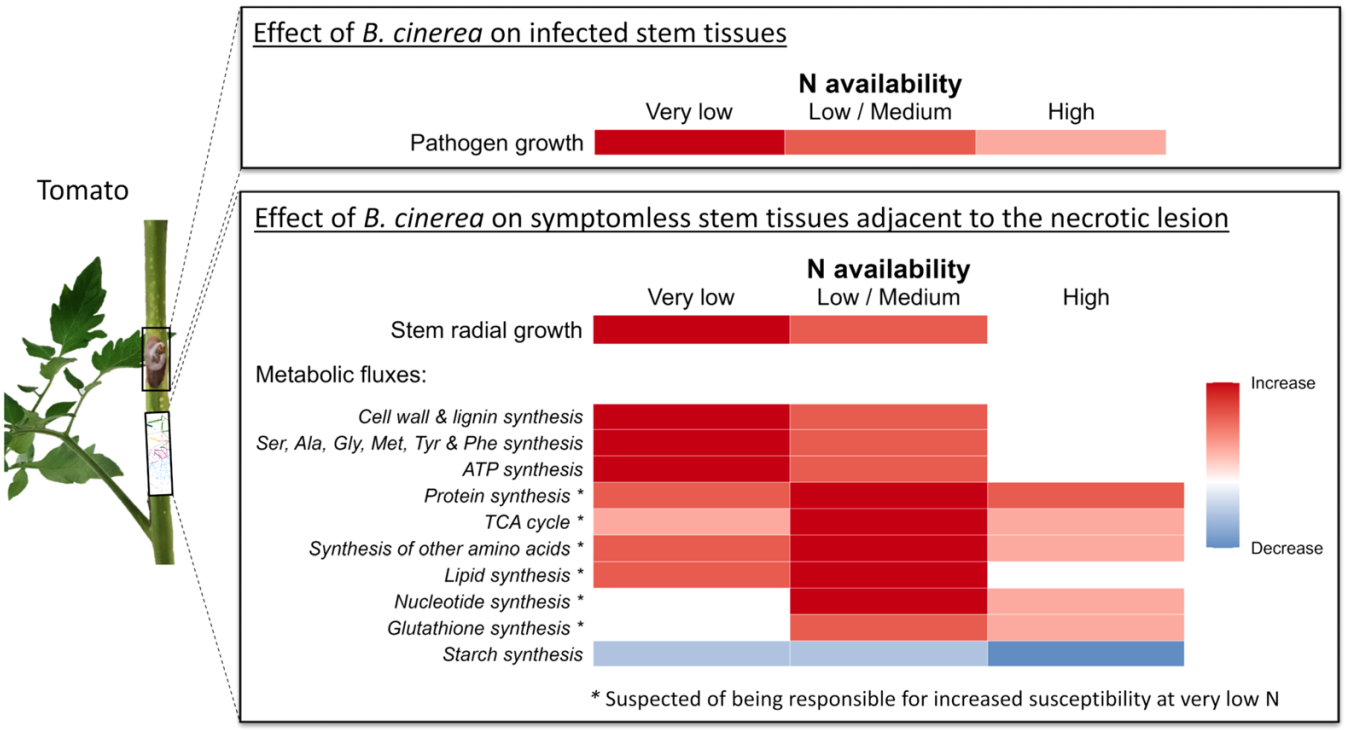

Fig. 8. Summary diagram of the main morphological and metabolic changes in tomato stems infected by *B. cinerea*. The growth rate of stem lesions varies according to the N nutrition of the host. At the margins of lesions, in symptomless areas, infection induces increased radial growth of the stem at very low, low, and medium N supplies. The weak development of the fungus under high N availability is associated with few changes in metabolic fluxes. Under lower N availability, fluxes are increased in most metabolic pathways compared with fluxes in mock-inoculated plants. However, in several pathways, under very low N availability, infection induces little or no additional flux. The absence of flux stimulation in these pathways could explain the increased sensitivity of the stem to very low N. The colours indicate the increase or decrease in flux in *Botrytis*-inoculated plants compared with mock-inoculated plants. These changes in flux intensities are the general trend observed, and do not give any indication of the value of the fluxes, which can vary greatly from one reaction to another, and from one pathway to another.

in primary and secondary metabolism, provided fungal development was sufficient to trigger responses. These higher fluxes in infected plants were dependent on resources coming from distal tissues and, in part, on sufficient N availability. That N favours defence in tomato but not in several other species suggests that N may also enhance as yet unknown susceptibility factors in some hosts, independently of the metabolic adaptations presented in this work. The coherence of observed biochemical adaptations and metabolic network modelling provides clues to better understand host adaptation in sink tissue after a necrotrophic infection, notably local growth that accompanies the increased metabolic demand for defence.

Supplementary data

The following supplementary data are available at *JXB* online.

Fig. S1. Modelled stem metabolic network.

Fig. S2. Time course of stem mass and protein and fructose contents after inoculation.

Fig. S3. Disease severity caused by *B. cinerea*.

Fig. S4. Carbon and nitrogen influx.

Fig. S5. Coordination within the metabolic network of mock-inoculated plants.

Fig. S6. Detail of flux Cluster 2 in *Botrytis*-inoculated plants.

Fig. S7. Detail of flux Cluster 1.2 in *Botrytis*-inoculated plants.

Table S1. List of the variables quantified in tomato stems and the methods used for quantification.

Table S2. Accumulated compounds and biomass components in tomato stem samples.

Table S3. Stem diameter and dry mass per unit of length.

Table S4. List of metabolites within the metabolic model.

Table S5. List of reactions within the metabolic model.

Table S6. Upper and lower bounds of flux values (in μmol cm^{-1} d^{-1}) used to constrain the resolution of the metabolic model.

Table S7. Standard deviation of the residuals of the regressions.

Table S8. Fluxes in tomato stems under four nitrate nutrition levels and inoculated with *Botrytis cinerea* or mock.

Table S9. Correlation matrix of fluxes in mock-inoculated plants.

Table S10. Correlation matrix of fluxes in *Botrytis*-inoculated plants.

Protocol S1. Details of the assumptions and simplifications in the metabolic model.

Protocol S2. SBML file of the metabolic model.

Acknowledgements

We thank F. De Bruyne, C. Troulet, M. Duffaud, L. Touloumet, C. Le Bourvellec, C. Cassan, and Y. Gibon for their expert technical assistance.

Author contributions

NL: performing all the experiments and metabolomics analyses, reconstructing the metabolic network, performing flux simulation, and contributing to data mining and article writing; FL and SC: design, performing data mining, and writing the article; RL and PN: contributing to the design; DD: analysing ascorbate, glutathione, asparagine, glutamine, glutamate, aspartate, and proline.

Conflict of interest

The authors declare that they have no conflicts of interest.

Funding

This study was conducted with the financial support of the European Regional Development Fund, the French government, the Sud Provence-Alpes-Côte d'Azur Region, the Departmental Council of Vaucluse, and the Urban Community of Avignon. NL was supported by a PhD fellowship from the Federative Research Structure Tersys Plateforme 3A.

Data availability

All relevant data to support the findings of this study can be found within the manuscript and its supporting data, and are openly available in Zenodo at https://doi.org/10.5281/zenodo.10851844 (Lacrampe *et al*., 2024)

References

Abro MA, Lecompte F, Bardin M, Nicot PC. 2014. Nitrogen fertilization impacts biocontrol of tomato gray mold. Agronomy for Sustainable Development **34**, 641–648.

Adrian M, Jeandet P, Veneau J, Weston LA, Bessis R. 1997. Biological activity of resveratrol, a stilbenic compound from grapevines, against *Botrytis cinerea*, the causal agent for gray mold. Journal of Chemical Ecology **23**, 1689–1702.

Aerts N, Pereira Mendes M, Van Wees SCM. 2021. Multiple levels of crosstalk in hormone networks regulating plant defense. The Plant Journal **105**, 489–504.

Agudelo-Romero P, Erban A, Rego C, Carbonell-Bejerano P, Nascimento T, Sousa L, Martínez-Zapater JM, Kopka J, Fortes AM. 2015. Transcriptome and metabolome reprogramming in *Vitis vinifera* cv. Trincadeira berries upon infection with *Botrytis cinerea*. Journal of Experimental Botany **66**, 1769–1785.

Badmi R, Tengs T, Brurberg MB, Elameen A, Zhang Y, Haugland LK, Fossdal CG, Hytönen T, Krokene P, Thorstensen T. 2022. Transcriptional profiling of defense responses to *Botrytis cinerea* infection in leaves of *Fragaria vesca* plants soil-drenched with β-aminobutyric acid. Frontiers in Plant Science **13**, 1025422.

Bahrami AR, Chen Z-H, Walker RP, Leegood RC, Gray JE. 2001. Ripening-related occurrence of phosphoenolpyruvate carboxykinase in tomato fruit. Plant Molecular Biology **47**, 499–506.

Benito EP, Ten Have A, Van'T Klooster JW, Van Kan JAL. 1998. Fungal and plant gene expression during synchronized infection of tomato leaves by *Botrytis cinerea*. European Journal of Plant Pathology **104**, 207–220.

Berger S, Papadopoulos M, Schreiber U, Kaiser W, Roitsch T. 2004. Complex regulation of gene expression, photosynthesis and sugar levels by pathogen infection in tomato. Physiologia Plantarum **122**, 419–428.

Bolton MD. 2009. Primary metabolism and plant defense—fuel for the fire. Molecular Plant-Microbe Interactions **22**, 487–497.

Brauc S, De Vooght E, Claeys M, Geuns JMC, Höfte M, Angenon G. 2012. Overexpression of arginase in *Arabidopsis thaliana* influences defence responses against *Botrytis cinerea*: arginase influences defence against *Botrytis*. Plant Biology **14**, 39–45.

Buxdorf K, Yaffe H, Barda O, Levy M. 2013. The effects of glucosinolates and their breakdown products on necrotrophic fungi. PLoS One **8**, e70771.

Camañes G, Scalschi L, Vicedo B, González-Bosch C, García-Agustín P. 2015. An untargeted global metabolomic analysis reveals the biochemical changes underlying basal resistance and priming in *Solanum lycopersicum*, and identifies 1-methyltryptophan as a metabolite involved in plant responses to *Botrytis cinerea* and *Pseudomonas syringae*. The Plant Journal **84**, 125–139.

Chassot C, Nawrath C, Métraux J-P. 2007. Cuticular defects lead to full immunity to a major plant pathogen: cuticle and immunity. The Plant Journal **49**, 972–980.

Clark TJ, Guo L, Morgan J, Schwender J. 2020. Modeling plant metabolism: from network reconstruction to mechanistic models. Annual Review of Plant Biology **71**, 303–326.

Collakova E, Yen JY, Senger RS. 2012. Are we ready for genome-scale modeling in plants? Plant Science **191–192**, 53–70.

Colombié S, Beauvoit B, Nazaret C, *et al*. 2017. Respiration climacteric in tomato fruits elucidated by constraint-based modelling. New Phytologist **213**, 1726–1739.

Colombié S, Nazaret C, Bénard C, *et al*. 2015. Modelling central metabolic fluxes by constraint-based optimization reveals metabolic reprogramming of developing *Solanum lycopersicum* (tomato) fruit. The Plant Journal **81**, 24–39.

Dean R, Van Kan JAL, Pretorius ZA, *et al*. 2012. The Top 10 fungal pathogens in molecular plant pathology. Molecular Plant Pathology **13**, 414–430.

De Cremer K, Mathys J, Vos C, Froenicke L, Michelmore RW, Cammue BPA, De Coninck B. 2013. RNAseq-based transcriptome analysis of *Lactuca sativa* infected by the fungal necrotroph *Botrytis cinerea*: lettuce transcriptome during *B. cinerea* infection. Plant, Cell & Environment **36**, 1992–2007.

Dersch LM, Beckers V, Wittmann C. 2016. Green pathways: metabolic network analysis of plant systems. Metabolic Engineering **34**, 1–24.

Dixon RA, Achnine L, Kota P, Liu C-J, Reddy MSS, Wang L. 2002. The phenylpropanoid pathway and plant defence—a genomics perspective: phenylpropanoids and plant defence. Molecular Plant Pathology **3**, 371–390.

Fagard M, Launay A, Clement G, Courtial J, Dellagi A, Farjad M, Krapp A, Soulie M-C, Masclaux-Daubresse C. 2014. Nitrogen metabolism meets phytopathology. Journal of Experimental Botany **65**, 5643–5656.

Fan Y, Yang W, Yan Q, Chen C, Li J. 2019. Genome-wide identification and expression analysis of the protease inhibitor gene families in tomato. Genes **11**, 1–22.

Ferrari S, Plotnikova JM, De Lorenzo G, Ausubel FM. 2003. *Arabidopsis* local resistance to *Botrytis cinerea* involves salicylic acid and camalexin and requires *EDS4* and *PAD2*, but not *SID2*, *EDS5* or *PAD4*: local *Arabidopsis* response to *Botrytis*. The Plant Journal **35**, 193–205.

Forde BG, Lea PJ. 2007. Glutamate in plants: metabolism, regulation, and signalling. Journal of Experimental Botany **58**, 2339–2358.

Fritsch FN, Carlson RE. 1980. Monotone piecewise cubic interpolation. SIAM Journal on Numerical Analysis **17**, 238–246.

Gerlin L, Cottret L, Escourrou A, Genin S, Baroukh C. 2022. A multi-organ metabolic model of tomato predicts plant responses to nutritional and genetic perturbations. Plant Physiology **188**, 1709–1723.

Goetz G, Fkyerat A, Métais N, Kunz M, Tabacchi R, Pezet R, Pont V. 1999. Resistance factors to grey mould in grape berries: identification of some phenolics inhibitors of *Botrytis cinerea* stilbene oxidase. Phytochemistry **52**, 759–767.

Guo Q, Major IT, Howe GA. 2018. Resolution of growth–defense conflict: mechanistic insights from jasmonate signaling. Current Opinion in Plant Biology **44**, 72–81.

Haile ZM, Pilati S, Sonego P, Malacarne G, Vrhovsek U, Engelen K, Tudzynski P, Zottini M, Baraldi E, Moser C. 2017. Molecular analysis of the early interaction between the grapevine flower and *Botrytis cinerea* reveals that prompt activation of specific host pathways leads to fungus quiescence: *Vitis vinifera* flower and *Botrytis cinerea* quiescence. Plant, Cell & Environment **40**, 1409–1428.

Hatmi S, Trotel-Aziz P, Villaume S, Couderchet M, Clément C, Aziz A. 2014. Osmotic stress-induced polyamine oxidation mediates defence responses and reduces stress-enhanced grapevine susceptibility to *Botrytis cinerea*. Journal of Experimental Botany **65**, 75–88.

Holzhütter H-G. 2006. The generalized flux-minimization method and its application to metabolic networks affected by enzyme deficiencies. Biosystems **83**, 98–107.

Hong Y-S, Martinez A, Liger-Belair G, Jeandet P, Nuzillard J-M, Cilindre C. 2012. Metabolomics reveals simultaneous influences of plant defence system and fungal growth in *Botrytis cinerea*-infected *Vitis vinifera* cv. Chardonnay berries. Journal of Experimental Botany **63**, 5773–5785.

Iriti M, Rossoni M, Borgo M, Faoro F. 2004. Benzothiadiazole enhances resveratrol and anthocyanin biosynthesis in grapevine, meanwhile improving resistance to *Botrytis cinerea*. Journal of Agricultural and Food Chemistry **52**, 4406–4413.

Kirkby EA, Knight AH. 1977. Influence of the level of nitrate nutrition on ion uptake and assimilation, organic acid accumulation, and cation–anion balance in whole tomato plants. Plant Physiology **60**, 349–353.

Kliebenstein DJ, Rowe HC, Denby KJ. 2005. Secondary metabolites influence *Arabidopsis*/*Botrytis* interactions: variation in host production and pathogen sensitivity: secondary metabolites influence *Arabidopsis*/*Botrytis* interactions. The Plant Journal **44**, 25–36.

Kumar V, Hatan E, Bar E, Davidovich-Rikanati R, Doron-Faigenboim A, Spitzer-Rimon B, Elad Y, Alkan N, Lewinsohn E, Oren-Shamir M. 2020. Phenylalanine increases chrysanthemum flower immunity against *Botrytis cinerea* attack. The Plant Journal **104**, 226–240.

Kuźniak E, Skłodowska M. 2005. Fungal pathogen-induced changes in the antioxidant systems of leaf peroxisomes from infected tomato plants. Planta **222**, 192–200.

Lacrampe N, Colombié S, Dumont D, Nicot P, Lecompte F, Lugan R. 2023. Nitrogen-mediated metabolic patterns of susceptibility to *Botrytis cinerea* infection in tomato (*Solanum lycopersicum*) stems. Planta **257**, 41.

Lacrampe N, Lopez-Lauri F, Lugan R, Colombié S, Olivares J, Nicot PC, Lecompte F. 2021. Regulation of sugar metabolism genes in the nitrogen-dependent susceptibility of tomato stems to *Botrytis cinerea*. Annals of Botany **127**, 143–154.

Lacrampe N, Lugan R, Dumont D, Nicot PC, Lecompte F, Colombié S. 2024. Data from: Modelling metabolic fluxes of tomato stems reveals that nitrogen shapes central metabolism for defence against *Botrytis cinerea*. Zenodo. https://doi.org/10.5281/zenodo.10851844

Lanver D, Müller AN, Happel P, *et al*. 2018. The biotrophic development of *Ustilago maydis* studied by RNA-Seq analysis. The Plant Cell **30**, 300–323.

Lecompte F, Abro MA, Nicot PC. 2013. Can plant sugars mediate the effect of nitrogen fertilization on lettuce susceptibility to two necrotrophic pathogens: *Botrytis cinerea* and *Sclerotinia sclerotiorum*? Plant and Soil **369**, 387–401.

Lecompte F, Nicot PC, Ripoll J, Abro MA, Raimbault AK, Lopez-Lauri F, Bertin N. 2017. Reduced susceptibility of tomato stem to the necrotrophic fungus *Botrytis cinerea* is associated with a specific adjustment of fructose content in the host sugar pool. Annals of Botany **119**, 931–943.

Li Y, Li S, Du R, Wang J, Li H, Xie D, Yan J. 2021. Isoleucine enhances plant resistance against *Botrytis cinerea* via jasmonate signaling pathway. Frontiers in Plant Science **12**, 628328.

Liao C-J, Hailemariam S, Sharon A, Mengiste T. 2022. Pathogenic strategies and immune mechanisms to necrotrophs: differences and similarities to biotrophs and hemibiotrophs. Current Opinion in Plant Biology **69**, 102291.

Lo Presti L, Lanver D, Schweizer G, Tanaka S, Liang L, Tollot M, Zuccaro A, Reissmann S, Kahmann R. 2015. Fungal effectors and plant susceptibility. Annual Review of Plant Biology **66**, 513–545.

Luna E, Flandin A, Cassan C, Prigent S, Chevanne C, Kadiri CF, Gibon Y, Pétriacq P. 2020. Metabolomics to exploit the primed immune system of tomato fruit. Metabolites **10**, 96.

Massot C, Bancel D, Lopez Lauri F, Truffault V, Baldet P, Stevens R, Gautier H. 2013. High temperature inhibits ascorbate recycling and light stimulation of the ascorbate pool in tomato despite increased expression of biosynthesis genes. PLoS One **8**, e84474.

Meister A, Anderson ME. 1983. Glutathione. Annual Review of Biochemistry **52**, 711–760.

Morales J, Mendoza L, Cotoras M. 2017. Alteration of oxidative phosphorylation as a possible mechanism of the antifungal action of *p*-coumaric acid against *Botrytis cinerea*. Journal of Applied Microbiology **123**, 969–976.

Mulema JMK, Denby KJ. 2012. Spatial and temporal transcriptomic analysis of the *Arabidopsis thaliana–Botrytis cinerea* interaction. Molecular Biology Reports **39**, 4039–4049.

Naets M, Van Hemelrijck W, Gruyters W, Verboven P, Nicolaï B, Keulemans W, De Coninck B, Geeraerd AH. 2022. Time is of the essence—early activation of the mevalonate pathway in apple challenged with gray mold correlates with reduced susceptibility during postharvest storage. Frontiers in Microbiology **13**, 797234.

Nambeesan S, AbuQamar S, Laluk K, Mattoo AK, Mickelbart MV, Ferruzzi MG, Mengiste T, Handa AK. 2012. Polyamines attenuate ethylene-mediated defense responses to abrogate resistance to *Botrytis cinerea* in tomato. Plant Physiology **158**, 1034–1045.

Ngou BPM, Ding P, Jones JDG. 2022. Thirty years of resistance: zig-zag through the plant immune system. The Plant Cell **34**, 1447–1478.

Oliva M, Hatan E, Kumar V, *et al*. 2020. Increased phenylalanine levels in plant leaves reduces susceptibility to *Botrytis cinerea*. Plant Science **290**, 110289.

Orth JD, Thiele I, Palsson BO. 2010. What is flux balance analysis? Nature Biotechnology **28**, 245–248.

Peyraud R, Cottret L, Marmiesse L, Gouzy J, Genin S. 2016. A resource allocation trade-off between virulence and proliferation drives metabolic versatility in the plant pathogen *Ralstonia solanacearum*. PLoS Pathogens **12**, e1005939.

Peyraud R, Mbengue M, Barbacci A, Raffaele S. 2019. Intercellular cooperation in a fungal plant pathogen facilitates host colonization. Proceedings of the National Academy of Sciences, USA **116**, 3193–3201.

Pfeiffer T, Sánchez-Valdenebro I, Nuño JC, Montero F, Schuster S. 1999. METATOOL: for studying metabolic networks. Bioinformatics **15**, 251–257.

Quidde T, Osbourn AE, Tudzynski P. 1998. Detoxification of α-tomatine by *Botrytis cinerea*. Physiological and Molecular Plant Pathology **52**, 151–165.

Rasul S, Dubreuil-Maurizi C, Lamotte O, Koen E, Poinssot B, Alcaraz G, Wendehenne D, Jeandroz S. 2012. Nitric oxide production mediates oligogalacturonide-triggered immunity and resistance to *Botrytis cinerea* in *Arabidopsis thaliana*: NO production in response to OGs. Plant, Cell & Environment **35**, 1483–1499.

Renard CMGC, Voragen AGJ, Thibault JF, Pilnik W. 1990. Studies on apple protopectin: I. Extraction of insoluble pectin by chemical means. Carbohydrate Polymers **12**, 9–25.

Rodenburg SYA, Seidl MF, Judelson HS, Vu AL, Govers F, De Ridder D. 2019. Metabolic model of the *Phytophthora infestans*–tomato interaction reveals metabolic switches during host colonization. mBio **10**, e00454–e00419.

Rojas CM, Senthil-Kumar M, Tzin V, Mysore KS. 2014. Regulation of primary plant metabolism during plant–pathogen interactions and its contribution to plant defense. Frontiers in Plant Science **5**, 1–12.

Rowe HC, Walley JW, Corwin J, Chan EK-F, Dehesh K, Kliebenstein DJ. 2010. Deficiencies in jasmonate-mediated plant defense reveal quantitative variation in *Botrytis cinerea* pathogenesis. PLoS Pathogens **6**, e1000861.

Ruan Y-L. 2014. Sucrose metabolism: gateway to diverse carbon use and sugar signaling. Annual Review of Plant Biology **65**, 33–67.

Salzman RA, Tikhonova I, Bordelon BP, Hasegawa PM, Bressan RA. 1998. Coordinate accumulation of antifungal proteins and hexoses constitutes a developmentally controlled defense response during fruit ripening in grape. Plant Physiology **117**, 465–472.

Seifi HS, Curvers K, Vleesschauwer D, Delaere I, Aziz A, Höfte M. 2013. Concurrent overactivation of the cytosolic glutamine synthetase and the GABA shunt in the ABA-deficient *sitiens* mutant of tomato leads to resistance against *Botrytis cinerea*. New Phytologist **199**, 490–504.

Sestari I, Campos ML. 2022. Into a dilemma of plants: the antagonism between chemical defenses and growth. Plant Molecular Biology **109**, 469–482.

Shao D, Smith DL, Kabbage M, Roth MG. 2021. Effectors of plant necrotrophic fungi. Frontiers in Plant Science **12**, 687713.

Silva CJ, Adaskaveg JA, Mesquida-Pesci SD, *et al*. 2023. *Botrytis cinerea* infection accelerates ripening and cell wall disassembly to promote disease in tomato fruit. Plant Physiology **191**, 575–590.

Silva CJ, Van Den Abeele C, Ortega-Salazar I, Papin V, Adaskaveg JA, Wang D, Casteel CL, Seymour GB, Blanco-Ulate B. 2021. Host susceptibility factors render ripe tomato fruit vulnerable to fungal disease despite active immune responses. Journal of Experimental Botany **72**, 2696–2709.

Smith JE, Mengesha B, Tang H, Mengiste T, Bluhm BH. 2014. Resistance to *Botrytis cinerea* in *Solanum lycopersicoides* involves widespread transcriptional reprogramming. BMC Genomics **15**, 334.

Soulie M, Koka SM, Floch K, *et al*. 2020. Plant nitrogen supply affects the *Botrytis cinerea* infection process and modulates known and novel virulence factors. Molecular Plant Pathology **21**, 1436–1450.

Stukkens Y, Bultreys A, Grec S, Trombik T, Vanham D, Boutry M. 2005. NpPDR1, a pleiotropic drug resistance-type ATP-binding cassette transporter from *Nicotiana plumbaginifolia*, plays a major role in plant pathogen defense. Plant Physiology **139**, 341–352.

Sun C, Jin L, Cai Y, Huang Y, Zheng X, Yu T. 2019. L-Glutamate treatment enhances disease resistance of tomato fruit by inducing the expression of glutamate receptors and the accumulation of amino acids. Food Chemistry **293**, 263–270.

Sweetlove LJ, Ratcliffe RG. 2011. Flux-balance modeling of plant metabolism. Frontiers in Plant Science **2**, 38.

Tarkowski LP, Signorelli S, Höfte M. 2020. γ-Aminobutyric acid and related amino acids in plant immune responses: emerging mechanisms of action. Plant, Cell & Environment **43**, 1103–1116.

The SV, Snyder R, Tegeder M. 2021. Targeting nitrogen metabolism and transport processes to improve plant nitrogen use efficiency. Frontiers in Plant Science **11**, 628366.

Thévenot EA, Roux A, Xu Y, Ezan E, Junot C. 2015. Analysis of the human adult urinary metabolome variations with age, body mass index, and gender by implementing a comprehensive workflow for univariate and OPLS statistical analyses. Journal of Proteome Research **14**, 3322–3335.

Thomma BPHJ, Eggermont K, Penninckx IAMA, Mauch-Mani B, Vogelsang R, Cammue BPA, Broekaert WF. 1998. Separate jasmonate-dependent and salicylate-dependent defense-response pathways in *Arabidopsis* are essential for resistance to distinct microbial pathogens. Proceedings of the National Academy of Sciences, USA **95**, 15107–15111.

Tsao R, Zhou T. 2000. Antifungal activity of monoterpenoids against postharvest pathogens *Botrytis cinerea* and *Monilinia fructicola*. Journal of Essential Oil Research **12**, 113–121.

Valle EM, Boggio SB, Heldt HW. 1998. Free amino acid composition of phloem sap and growing fruit of *Lycopersicon esculentum*. Plant and Cell Physiology **39**, 458–461.

Vega A, Canessa P, Hoppe G, Retamal I, Moyano TC, Canales J, Gutiérrez RA, Rubilar J. 2015. Transcriptome analysis reveals regulatory networks underlying differential susceptibility to *Botrytis cinerea* in response to nitrogen availability in *Solanum lycopersicum*. Frontiers in Plant Science **6**, 911.

Veloso J, Van Kan JAL. 2018. Many shades of grey in *Botrytis*–host plant interactions. Trends in Plant Science **23**, 613–622.

Wang Y, Pruitt RN, Nürnberger T, Wang Y. 2022. Evasion of plant immunity by microbial pathogens. Nature Reviews. Microbiology **20**, 449–464.

Weaver LM, Amasino RM. 2001. Senescence is induced in individually darkened *Arabidopsis* leaves, but inhibited in whole darkened plants. Plant Physiology **127**, 876–886.

Westrick NM, Ranjan A, Jain S, Grau CR, Smith DL, Kabbage M. 2019. Gene regulation of *Sclerotinia sclerotiorum* during infection of *Glycine max*: on the road to pathogenesis. BMC Genomics **20**, 157.

Williams TCR, Poolman MG, Howden AJM, Schwarzlander M, Fell DA, Ratcliffe RG, Sweetlove LJ. 2010. A genome-scale metabolic model accurately predicts fluxes in central carbon metabolism under stress conditions. Plant Physiology **154**, 311–323.

Windram O, Madhou P, McHattie S, *et al*. 2012. *Arabidopsis* defense against *Botrytis cinerea*: chronology and regulation deciphered by high-resolution temporal transcriptomic analysis. The Plant Cell **24**, 3530–3557.

Xiao G, Zhang Q, Zeng X, Chen X, Liu S, Han Y. 2022. Deciphering the molecular signatures associated with resistance to *Botrytis cinerea* in strawberry flower by comparative and dynamic transcriptome analysis. Frontiers in Plant Science **13**, 888939.

Xiong J-S, Zhu H-Y, Bai Y-B, Liu H, Cheng Z-M. 2018. RNA sequencing-based transcriptome analysis of mature strawberry fruit infected by necrotrophic fungal pathogen *Botrytis cinerea*. Physiological and Molecular Plant Pathology **104**, 77–85.

Yermiyahu U, Shamai I, Peleg R, Dudai N, Shtienberg D. 2006. Reduction of *Botrytis cinerea* sporulation in sweet basil by altering the concentrations of nitrogen and calcium in the irrigation solution. Plant Pathology **55**, 544–552.

You Y, Kan JAL. 2021. Bitter and sweet make tomato hard to (b)eat. New Phytologist **230**, 90–100.

Yuan H, Cheung CYM, Poolman MG, Hilbers PAJ, Riel NAW. 2016. A genome-scale metabolic network reconstruction of tomato (*Solanum lycopersicum* L.) and its application to photorespiratory metabolism. The Plant Journal **85**, 289–304.

Yurkovich JT, Palsson BO. 2016. Solving puzzles with missing pieces: the power of systems biology. Proceedings of the IEEE **104**, 2–7.

Zeier J. 2013. New insights into the regulation of plant immunity by amino acid metabolic pathways: amino acid metabolism and plant immunity. Plant, Cell & Environment **36**, 2085–2103.

Zhang Y, De Stefano R, Robine M, Butelli E, Bulling K, Hill L, Rejzek M, Martin C, Schoonbeek H. 2015. Different ROS-scavenging properties of flavonoids determine their abilities to extend shelf life of tomato. Plant Physiology **169**, 1568–1583.

Zheng Z, Qamar SA, Chen Z, Mengiste T. 2006. *Arabidopsis* WRKY33 transcription factor is required for resistance to necrotrophic fungal pathogens. The Plant Journal **48**, 592–605.